The Astrophysical Journal, 944:104 (18pp), 2023 February 10 https://doi.org/10.3847/1538-4357/acaf7c

Solar Flare Ribbon Fronts. I. Constraining Flare Energy Deposition with IRIS Spectroscopy

Vanessa Polito[1,2,3], Graham S. Kerr[4,5], Yan Xu[6,7], Viacheslav M. Sadykov[8], and Juraj Lorincik[1,2]
[1] Bay Area Environmental Research Institute, NASA Research Park, Moffett Field, CA 94035-0001, USA; polito@baeri.org
[2] Lockheed Martin Solar and Astrophysics Laboratory, Building 252, 3251 Hanover Street, Palo Alto, CA 94304, USA
[3] Department of Physics, Oregon State University, 301 Weniger Hall, Corvallis, OR 97331, USA
[4] NASA Goddard Space Flight Center, Heliophysics Sciences Division, Code 671, 8800 Greenbelt Rd., Greenbelt, MD 20771, USA
[5] Department of Physics, Catholic University of America, 620 Michigan Avenue, Northeast, Washington, DC 20064, USA
[6] Institute for Space Weather Sciences, New Jersey Institute of Technology, 323 Martin Luther King Boulevard, Newark, NJ 07102-1982, USA
[7] Big Bear Solar Observatory, New Jersey Institute of Technology, 40386 North Shore Lane, Big Bear City, CA 92314-9672, USA
[8] Physics & Astronomy Department, Georgia State University, 25 Park Place NE, Atlanta, GA 30303, USA
Received 2022 October 3; revised 2022 December 8; accepted 2023 January 1; published 2023 February 15

Abstract

Spectral lines formed at lower atmospheric layers show peculiar profiles at the "leading edge" of ribbons during solar flares. In particular, increased absorption of the BBSO/GST He I λ10830 line, as well as broad and centrally reversed profiles in the spectra of the Mg II and C II lines observed by the IRIS satellite, has been reported. In this work, we aim to understand the physical origin of such peculiar IRIS profiles, which seem to be common of many, if not all, flares. To achieve this, we quantify the spectral properties of the IRIS Mg II profiles at the ribbon leading edge during four large flares and perform a detailed comparison with a grid of radiative hydrodynamic models using the RADYN+FP code. We also studied their transition region (TR) counterparts, finding that these ribbon front locations are regions where TR emission and chromospheric evaporation are considerably weaker compared to other parts of the ribbons. Based on our comparison between the IRIS observations and modeling, our interpretation is that there are different heating regimes at play in the leading edge and the main bright part of the ribbons. More specifically, we suggest that bombardment of the chromosphere by more gradual and modest nonthermal electron energy fluxes can qualitatively explain the IRIS observations at the ribbon leading front, while stronger and more impulsive energy fluxes are required to drive chromospheric evaporation and more intense TR emission in the bright ribbon. Our results provide a possible physical origin for the peculiar behavior of the IRIS chromospheric lines in the ribbon leading edge and new constraints for the flare models.

Unified Astronomy Thesaurus concepts: Solar flares (1496); Solar atmosphere (1477); Solar chromosphere (1479); Solar activity (1475)

Supporting material: animations

1. Introduction

During solar flares, magnetic reconnection liberates energy from the stressed coronal magnetic field (Priest & Forbes 2002; Janvier et al. 2013). This energy manifests in several forms, including the acceleration of large amounts of particles, but is ultimately radiated away (e.g., Emslie et al. 2012). Flares are characterized by this intense broadband enhancement to the solar radiative output, and it is through careful study of that radiation that we can extract information about the magnetic reconnection, energy release, and particle acceleration processes that occur during flares.

Flare energy is carried by some agent from the release site in corona to the lower atmosphere—the chromosphere and transition region (TR)—where it produces ribbon-like structures observable in the UV, optical, and near-infrared (e.g., Fletcher et al. 2011). This agent is typically thought to be nonthermal electrons, due to the almost ubiquitous presence of compact hard X-ray (HXR) sources that are spatially associated with chromospheric/TR ribbons (Holman et al. 2011; Fletcher et al. 2011; Kontar et al. 2011). Other mechanisms that are likely acting include nonthermal protons or heavier ions (e.g., Ramaty & Mandzhavidze 2000; Emslie et al. 2012), the conductive heat flux resulting from direct heating in the corona (e.g., Brosius 2012; Ashfield & Longcope 2021), or magneto-hydrodynamic (MHD) waves such as Alfvén waves (e.g., Fletcher & Hudson 2008; Reep & Russell 2016; Kerr et al. 2016; Reep et al. 2018b), though these alternative mechanisms are not as well characterized as the "electron beam" model. See also the discussion in Section 5.4 of Cheung et al. (2022).

While HXR observations to date offer relatively coarse spatial resolution (e.g., RHESSI had a spatial resolution of $\sim$2.″3 up to 100 keV and $\sim$7″ up to 400 keV; Lin et al. 2002), there is now a wealth of high spatial resolution observations of the lower atmosphere in the optical, UV, and near-infrared, both ground and space based. Two examples relevant for the research discussed in this manuscript are the Interface Region Imaging Spectrograph (IRIS; De Pontieu et al. 2014) and the Goode Solar Telescope at the Big Bear Solar Telescope (BBSO/GST; Goode & Cao 2012). IRIS offers spatial resolution of 0.″3–0.″4 in the far-UV (FUV) and near-UV (NUV), providing both images and spectra. BBSO/GST also provides imaging and spectra, but in the optical and near-infrared, where the diffraction limit of its 1.6 m telescope is 0.″08 at 500 nm and 0.″16 at 1 μm. These high-resolution observations have revealed in recent years that the very narrow

(few hundred kilometers) region ahead of the main bright part of the ribbon ("leading edge" or "ribbon fronts") exhibits features that differ from the brighter part of the ribbons.

Ribbon leading edges are thought to be the footpoints of the newest reconnected flare loops and therefore carry vital information about the energy transport and dissipation mechanisms and thus the energy release and particle acceleration processes themselves.

We focus on two examples of ribbon leading edge behavior that offer scope for fruitful diagnostics of energy deposition: the dimming of ribbons observed in He I λ10830, and the presence of unique spectral shapes of the Mg II NUV spectral lines.

Spectral lines of orthohelium (the He I λ10830 and He I D3 lines) have been observed to, curiously, undergo periods of *dimming* during solar flares, before brightening (e.g., Zirin 1980; Liu et al. 2013; Xu et al. 2016; Kobanov et al. 2018; Xu et al. 2022). This has been seen in both imaging and spectroscopy (Xu et al. 2016, 2022). Recent BBSO/GST observations showed that some of these dimmings occur along the leading edge of propagating flare ribbons (Xu et al. 2016, 2022), i.e., immediately following the injection of flare energy. These "negative" flare ribbons persisted for several dozens of seconds to over a minute, with a width of ~350–500 km. In addition, in the two-ribbon flares studied by Xu et al. (2016), only one ribbon in each flare exhibited the dimming, from which we can infer that energy deposition into each ribbon differed in some regard.

Clearly such observations suggest that the initial energy deposition into the chromosphere produced a response that differs from the typical expectation (that is, rapid impulsive brightening). Two suggestions were made: (1) that enhanced extreme-UV (EUV) radiation from the flare-heated corona increased the photoionization rate of He I, with subsequent recombinations to orthohelium and increased opacity that absorbed photospheric radiation (the photoionization–recombination mechanism (PRM)), or (2) that nonthermal electrons within the beam collisionally ionized He I, which subsequently recombined and overpopulated orthohelium sufficiently to absorb more photospheric radiation (the collisional ionization–recombination mechanism (CRM)).

Using field-aligned radiation hydrodynamic (RHD) modeling, Huang et al. (2020) and Kerr et al. (2021) showed that electron-beam-driven flare simulations could produce the observed pattern of dimming followed by brightening. Kerr et al. (2021) demonstrated that simulations that only included the PRM were unable to produce dimming of He I but simulations that also included nonthermal collisional ionization of He I were successful in producing dimming of the λ10830 line at flare onset. The characteristics of that dimming were related to the properties of the injected nonthermal electron distribution.

The results of Kerr et al. (2021) suggest that where we observe dimming of He I λ10830 ribbon fronts, followed by brightenings, nonthermal particles are present in the chromosphere. A harder nonthermal electron energy spectrum (larger proportion of higher-energy nonthermal electrons compared to lower-energy nonthermal electrons) and weaker flux of those electrons resulted in stronger, more sustained dimming. However, the lifetime of the dimming (i.e., the time during which a particular area existed as a "ribbon leading edge" source) was not consistent with observations. We were only able to model enhanced absorption for a few seconds, compared to several dozen seconds observed by Xu et al. (2016).

Routine high-resolution observations of the Sun in the FUV and NUV have been available since the launch of IRIS in 2013, and since then many hundreds of flares have been observed. One of the strongest sets of lines observed by IRIS are the Mg II *h* and *k* resonance lines and the Mg II subordinate triplet. Forming over a range of chromospheric altitudes, altogether these lines are diagnostically important (see, e.g., the quiet-Sun diagnostics of Leenaarts et al. 2013a, 2013b; Pereira et al. 2013). Modern inversion codes coupled with machine-learning techniques also mean that it is possible to estimate the atmospheric stratification of temperature, electron density, and other plasma properties from these lines (Sainz Dalda et al. 2019).

In flares, however, the Mg II lines appear very different from their quiescent counterparts (e.g., Kerr et al. 2015; Graham & Cauzzi 2015; Liu et al. 2015; Panos et al. 2018; Graham et al. 2020), making extracting the information they carry more troublesome. Sources within the bright flare ribbons are typically single peaked (in contrast to the central reversal commonplace elsewhere), broadened, very intense, redshifted, or with marked wing asymmetries and show non-Gaussian line wings (they can appear quite Lorentzian). At the same time, the subordinate lines go into emission, and the line ratios can be observed to decrease slightly (likely due to some opacity changes).

Attempts to model these lines in flares (e.g., Kerr et al. 2016; Rubio da Costa & Kleint 2017; Kerr et al. 2019a, 2019b; Huang et al. 2019; Zhu et al. 2019) have shown that high densities are required to "fill in" the central reversal, that chromospheric condensations can produce redshifts and asymmetric flows, and that turbulent broadening is likely not the main culprit behind the excess line widths (though we are still unable to sufficiently broaden the lines comparable to observations). During flares, the subordinate lines have also been found to form higher in altitude, forming close to the resonance lines (Kerr et al. 2019c; Zhu et al. 2019) so that their being in emission is not necessarily a sign of deep heating as is the case in the quiet Sun (e.g., Pereira et al. 2015).

Since IRIS has observed hundreds of thousands of individual Mg II spectra from many flares, it is advantageous to perform clustering techniques such as *k*-means in order to sift through this vast data set and identify commonalities that might otherwise be missed. This was performed initially for one flare by Xu et al. (2016), who noted that ribbon leading edge Mg II profiles showed marked differences compared to the brighter portions of the ribbon. This was greatly expanded on by Panos et al. (2018), who analyzed 33 M- and X-class flares. They found that in addition to the single-peaked "flare" profiles described above, there was a class of Mg II profiles that were located at the leading edge of some propagating ribbon sources (with variable lifetimes, but on the order of 1–3 minutes; Panos et al. 2021; Panos & Kleint 2021). Those ribbon front profiles had deep central reversals and slightly blueshifted cores, were extremely broad, and showed subordinate lines in emission. While Panos et al. (2018) and Tei et al. (2018) (who observed similar features in a C-class flare kernel) speculate that these could be caused by superposition of very strong unresolved flows at different chromospheric temperatures, enhanced turbulence at the leading edge of flare ribbons, or rising cool

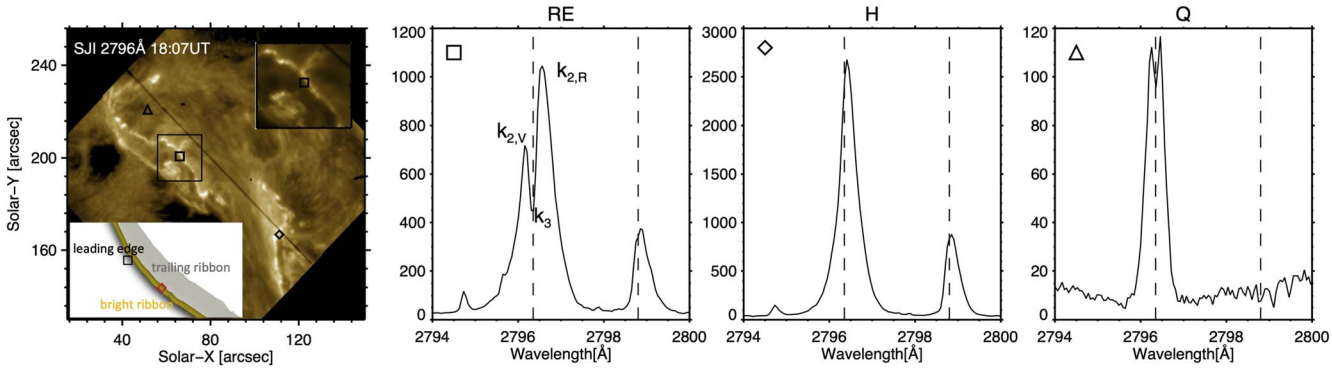

Figure 1. Overview of different types of Mg II profiles and their location within the flare (panel (a)). Examples of "ribbon leading edge" (RE; panel (b)) profiles (e.g., Panos et al. 2018); "heating" single-peaked profiles (H; panel (c)), which are more typical of the main bright ribbon; and a"quiet" nonflaring (Q; panel (d)) profile are given for comparison. The inset in the upper right corner of the left panel shows a zoomed-in view of one of the ribbons, where the example ribbon edge profile is taken. The inset in the lower left corner shows a cartoon illustrating the different locations across the ribbon. In the RE panel we note the common definition of the Mg II profiles k3 (line core) and k2v and k2r (flanking emission peaks on the blue and red side of the line core).

chromospheric material, there has been no self-consistent flare modeling that has explained these observations.

Finally, we briefly note other behaviors that illustrate the importance of studying flare ribbon fronts, and ribbons generally, in order to understand fundamental flare processes. Using IRIS slit-jaw imager (SJI) images in the FUV, Naus et al. (2022) found that while the ribbons are globally laminar, they contain fine-scale structure in both space and time. Ribbon front widths varied over time and were seen to activate some 1–3 minutes (in an average sense) before reaching peak intensity. This fine-scale structuring may be related directly to dynamics in the current sheet itself. Similarly, French et al. (2021) used very high cadence (1.7 s) IRIS data to relate flare ribbon dynamics to current sheet instabilities. From that same data set, Jeffrey et al. (2018) previously demonstrated that Si IV line widths increased prior to a strong increase in line intensity. The buildup of MHD turbulence during the early phases of ribbon development was posited as an explanation.

Here we continue our exploration of flare ribbon fronts that we started in Kerr et al. (2021), by determining whether the same models that could produce He I λ10830 dimming can produce Mg II NUV spectra consistent with IRIS ribbon front observations. To facilitate that comparison, we put the characteristics of the Mg II NUV ribbon front spectra on a more quantitative footing, building metrics that describe the centroid shifts, central reversal depths, and peak asymmetry, among others.

In Section 2 we quantify the characteristics of Mg II leading edge profiles observed by IRIS, and in Section 3 we synthesize Mg II NUV spectra, before performing a model–data comparison of the line metrics in Section 4. We do not address the line formation properties or ribbon front lifetimes here, leaving that to a follow-up work (Kerr et al. 2023, in preparation).

2. IRIS Observations of Flare Ribbons

In this section we describe the methodology we use to quantify the spectral characteristics of the IRIS Mg II ribbon leading edge (RE; Figure 1) profiles, which we will compare with the predictions from the RHD models in Section 3. Given that different terminologies have been used to refer to different ribbon locations in the literature, Figure 1 also illustrates the terminology that we choose to adopt throughout this paper. Specifically, we call the "leading edge (RE)," or ribbon front, the very narrow (few hundred kilometers) region where the peculiar Mg II profiles and enhanced absorption have been observed (see references in Section 1). This ribbon front region is immediately ahead of what we refer to as the "main bright ribbon." A typical Mg II profile in the latter part is shown in Figure 1 (e.g., "heating," or "H" profile). Finally, behind the main bright ribbon is the "fuzzy" ribbon emission that we call the "trailing ribbon." These different regions are also shown in the cartoon in the leftmost panel of Figure 1.

Since its launch in 2013, IRIS has provided an unprecedented view of the solar atmosphere from the photosphere to the flaring corona (De Pontieu et al. 2014, 2021). The satellite consists of a spectrograph and an SJI observing the Sun in both the FUV and NUV ranges at unprecedented spatial (0.″33–0.″4), temporal (down to 1 s or less), and spectral (2.7 km s^{-1} pixels) resolution. The IRIS spectrograph observes continua and spectral lines formed over a broad range of temperatures ($\log T$[K] ≈3.5–7) in both sit-and-stare and raster modes. The IRIS rasters can be (1) dense, if the raster step size is the same as the slit width (0.″33); (2) sparse, if the step size is 1″; or (3) coarse, if the step size is 2″.

We analyze a sample of four different flares observed by IRIS:

1. Flare 1: 2014 August 1 M-class flare (FL1; Figure 2): large and dense 64-step raster with cadence of ≈33 minutes, exposure time of ≈30 s, and step cadence of ≈32 s. This flare was analyzed by Xu et al. (2016), who observed enhanced absorption in the GST He I line and strongly reversed IRIS Mg II profiles at the edge of one of the ribbons (see also Section 1). We analyze the same raster as that in Xu et al. (2016), from ≈15:55 to 18:28 UT, where the RE profiles are observed.
2. Flare 2: 2015 June 22 M-class flare (FL2; Figure 3): large and sparse 16-step raster with raster cadence of ≈30 s, average exposure time of ≈1 s (down to ≈0.4 s for the NUV lines), and step cadence of ≈2 s. The spectrograph's observation has a spatial and spectral (for both the FUV and NUV channels) binning of 2 and is rotated by 45°. We analyze several rasters covering about 20 minutes around the flare's peak time, from ≈17:51 to 18:10 UT.
3. Flare 3: 2014 September 10 X-class flare (FL3; Figure 4): large sit-and-stare observation with exposure time of ≈8 s and cadence of ≈9 s with a spectral binning of 2 for the

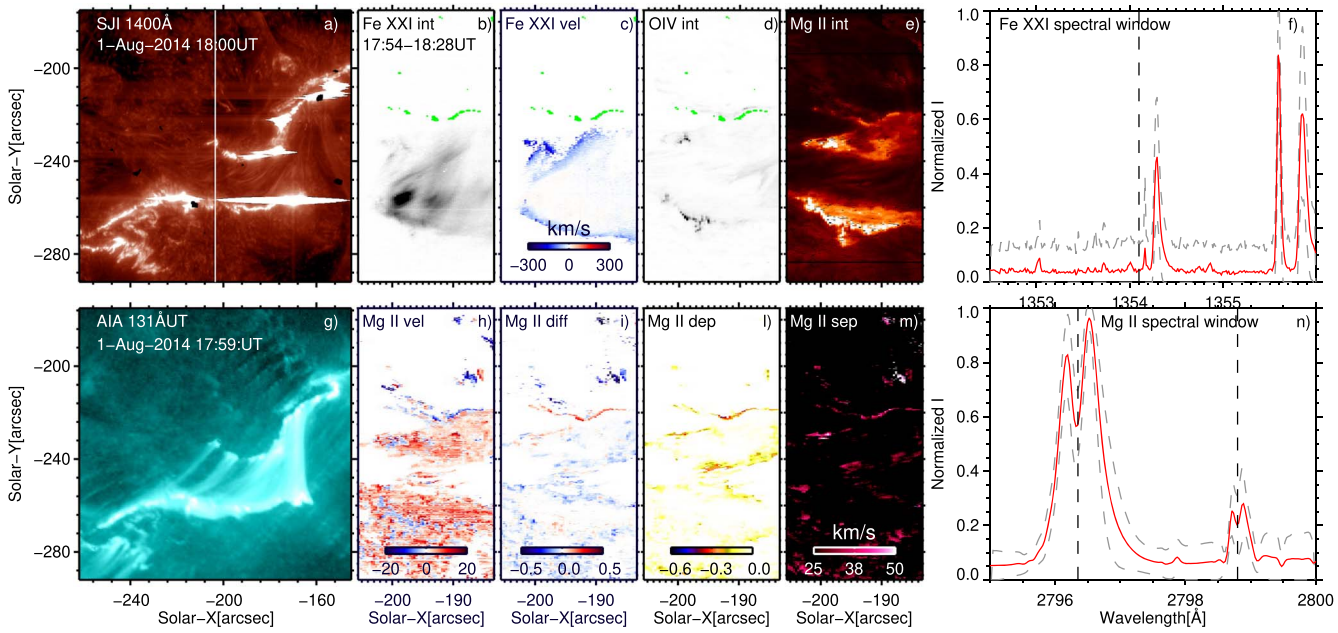

Figure 2. Overview of FL1: IRIS SJI 1400 Å image with raster FOV overlaid (panel (a)); Fe XXI intensity (panel (b)) and velocity (panel (c)); O IV intensity (panel (d)) from single-Gaussian fits with the contours of the pixels with the RE profiles in green overlaid; Mg II k3 intensity (panel (e)) and velocity (panel (h)); k2 peak difference (panel (i)); depth of central reversal (panel (l)); and k2 peak separation (panel (m)); see formulae in the main text. Panels (f) and (n) show the average spectra (red line) ± the standard deviation (gray dotted line) in the RE pixel locations for the Fe XXI and Mg II *k* windows, respectively. Panel (g) shows an overview of the flare in the AIA 131 Å filter. The time in panel (b) refers to the start and end time of the raster.

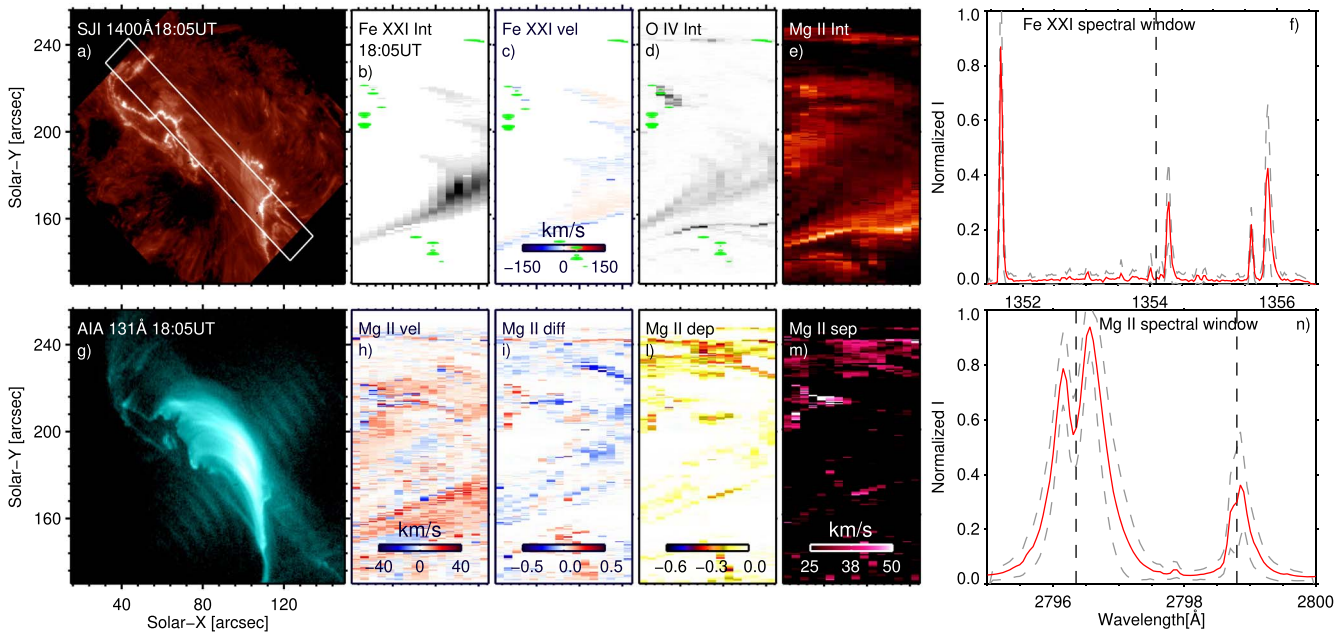

Figure 3. Overview of FL2 (one example raster): for the panels' description, see Figure 2 and Section 2. This observation had a rotation angle of 45°, but the raster data in panels (b)–(e) and (h)–(m) are not rotated for convenience. The time in panel (b) refers to the mid-time of the example raster (the raster cadence is ≈32 s). A movie associated with this figure is also available. The movie has a duration of 7 s and consists of a sequence of individual figures organized in the same exact way as the screenshot above, showing the evolution of the flare from 17:51 UT to 18:10 UT.

(An animation of this figure is available.)

FUV channel. We analyze about 20 minutes of the sit-and-stare observation from a start time of ≈17:25 UT.

4. Flare 4: 2014 October 27 X-class flare (FL4, Figure 5): large and coarse eight-step raster with raster cadence of ≈26 s, exposure time of 2 s (down to ≈0.26 and 0.64 s for the FUV and NUV lines, respectively), and step cadence of ≈3 s. The observation has a spatial and spectral (for both the FUV and NUV channels) binning of 2 and a rotation angle of 90°. We analyze several rasters covering about 18 minutes around the flare's peak time, from ≈14:14 to 14:32 UT.

Figures 2–5 show an overview of FL1–FL4, respectively. For each figure, we are showing an overview of the flare as observed by the IRIS SJI 1400 Å (dominated by Si IV emission at $T \approx$ 80 kK) or 1330 Å (dominated by C II emission at

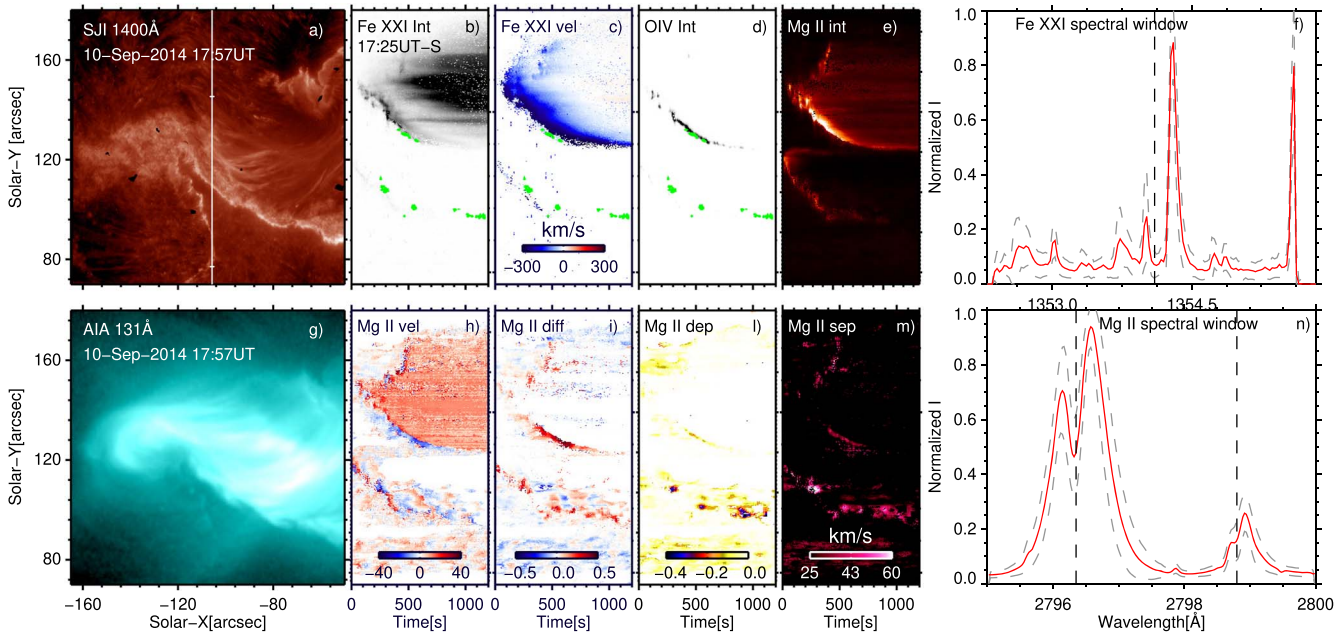

Figure 4. Overview of FL3; for the panels' description, see Figure 2 and Section 2. The time in panel (b) refers to the start time of the sit-and-stare observation shown here. The time in the *x*-axis for panels (b)–(e) and (h)–(m) is in seconds after the start time. Panels (b)–(e) and (h)–(m) show a portion of the sit-and-stare observation across the slit, which is highlighted by two small horizontal marks on the slit in panel (a).

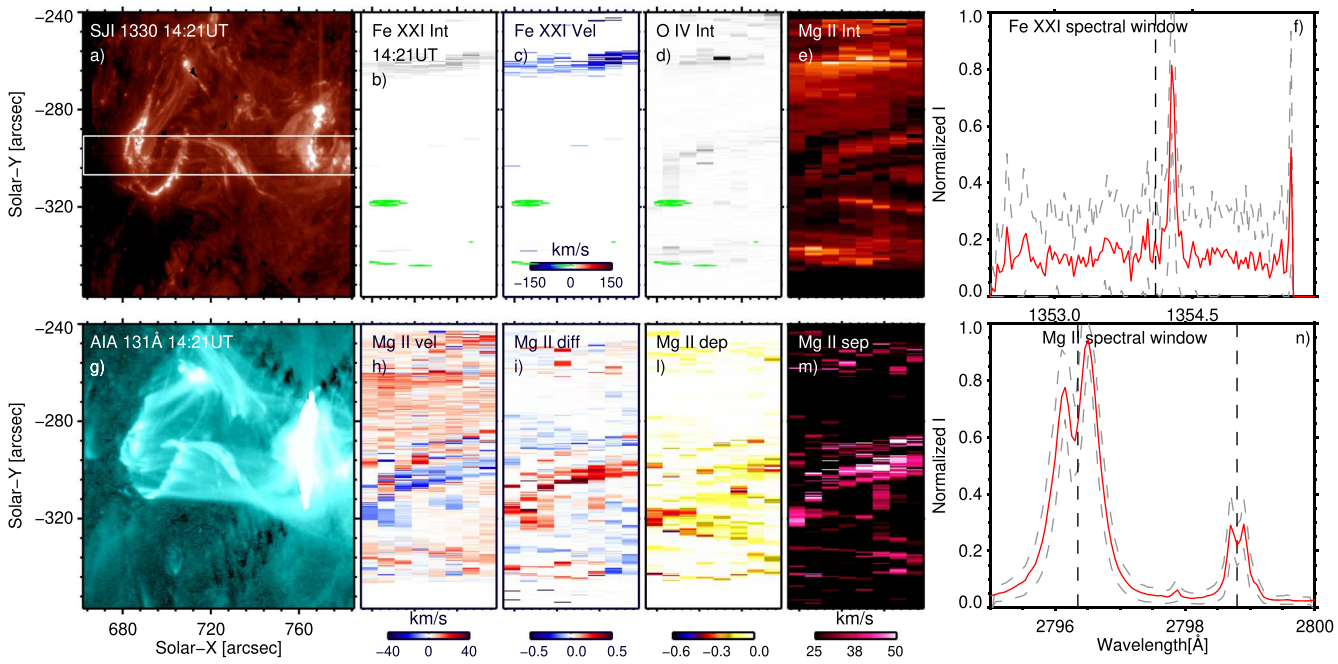

Figure 5. Overview of FL4 (one example raster); for the panels' description, see Figure 2 and Section 2. This observation had a rotation angle of 90°, but the raster data in panels (b)–(e) and (h)–(m) are not rotated for convenience. The time in panel (b) refers to the mid-time of the example raster (the raster cadence is ≈26 s). A movie associated with this figure is also available. The movie has a duration of 9 s and consists of a sequence of individual figures organized in the same exact way as the screenshot above, showing the evolution of the flare from 14:13 UT to 14:32 UT.

(An animation of this figure is available.)

$T \approx 10$–40 kK) filters (panel (a)) and the AIA 131 Å filter (which is dominated by Fe XXI emission at around 10 MK; panel (g)). Panels (b)–(e) and (h)–(m) show the spectrograph raster data within the field of view (FOV), which is overlaid on the SJI image in panel (a). For FL3, Figure 4 shows the data across a portion of the slit (which is highlighted by two small horizontal marks in panel (a)) as a function of time. FL2 and FL4 are rotated by 45° and 90°, respectively, but the raster data shown in Figure 3 and 5 are not rotated for convenience. The spectrograph data in panels (b)–(e) and (h)–(m) show Fe XXI intensity (panel (b)) and velocity (panel (c)), O IV intensity (panel (d)) obtained by performing single-Gaussian fits in each pixel, Mg II k3 intensity (panel (e)) and velocity (panel (h)), k_2 peak difference "diff" (panel (i)), depth of central reversal from the blue peak (i.e., "dep"; panel (l)), and k_2 peak separation ("sep"; panel (m)). We defined diff, dep,

and sep using the following formulae:

$$\mathrm{diff} = \frac{I_{k2,R} - I_{k2,V}}{I_{k2,R} + I_{k2,V}} \quad (1)$$

$$\mathrm{dep} = -\frac{I_{k2,V} - I_{k3}}{I_{k2,V} + I_{k3}} \quad (2)$$

$$\mathrm{sep} = v_{k2,R} - v_{k2,V}, \quad (3)$$

where I/v_{k3}, $I/v_{k2,V}$, and $I/v_{k2,R}$ are the intensity and Doppler velocities of the line core, blue peak, and red peak of the Mg II k line, respectively (see Figure 1). For each data set, we obtained these values using the `iris_get_mg_features_lev2` routine available within the IRIS solar software (SSW) package and described in Pereira et al. (2013). Although this is an automatic method to detect the Mg II line peaks, we also verified manually that it succeeded in fitting the RE profiles satisfactorily, in particular the line red and blue peaks and the line core.

The green contours in Figures 2–5 represent the location of the Mg II RE profiles that satisfy the criteria that we describe in Section 2.1. Finally, the red continuous spectra shown in panels (f) and (n) were obtained by averaging the spectra in the pixels indicated by the green contours for the Fe XXI and Mg II spectral windows, respectively, while the gray dotted spectra indicate the 1σ standard deviation of the averaged spectra.

2.1. Method to Identify and Characterize Ribbon Front Profiles

After calculating the spectral parameters for the Mg II line profiles as defined above, we identified the RE profiles by using the following metrics:

$$\mathrm{diff} \gtrsim 0 \quad (4)$$

$$I_{k2,V} \gtrsim 0.8\, I_{k3} \quad (5)$$

$$\mathrm{sep} \gtrsim 30 \text{ km s}^{-1} \quad (6)$$

$$I_{m,t} \gtrsim 20\%\, I_{m,k}, \quad (7)$$

where $I_{m,t}$ and $I_{m,k}$ represent the maximum emission in the Mg II triplet and k line spectra, respectively. Such metrics were defined based on the following:

1. the values we found in the RE profile representative group by performing a k-means analysis for one of the flares (FL2) analyzed in this work; and
2. the range of values found in Figure 7 of Panos & Kleint (2021), who used machine-learning techniques to obtain the most probable RE profiles for dozens of IRIS flares.

While a thorough machine-learning analysis for the four flares analyzed in this work is outside the scope of this paper (as it has been already presented in the series of papers by Panos et al.), method 1 allows us to put the RE metrics on a more quantitative basis, complementing the more qualitative overview presented in Xu et al. (2016) and Panos et al. (2018). Nevertheless, we verified that the two methods held good agreement, and we used a conservative approach when defining the metrics above, to ensure that the range of most probable RE profiles in Figure 7 of Panos & Kleint (2021) would be included by our metrics and that we are not losing important information on RE profiles.

We note that our analysis does not distinguish between different groups of RE profiles that are discussed in Panos's analysis, e.g., groups 11, 12, and 52 in Figure 3 of Panos et al. (2018), as well as "strong" and "weak" RE profiles in Figure 7 of Panos et al. (2021). This means that our averaged profiles in Figures 2–5 might show less pronounced features (in particular depth of the central reversal and peak separation) than those in group 52 or the "strong" RE profiles presented in those papers. We also note that the more extreme profiles (or group 52) are not as common as the weaker RE profiles (or groups 11–12), as can be seen in Figure 8 of Panos et al. (2018). In particular, flares 22, 29, and 31 in that figure correspond to our flares FL2, FL3, and FL4, respectively. We note that our FL3 has the lowest incidence of strong RE profiles, while FL2 has the largest. Even then, the "weaker" RE profiles (closer to our average profiles in Figures 2–5) dominate.

Figures 2–5 show that the profiles identified by these criteria are indeed found in the ribbon leading edge. In addition, we note that Fe XXI and O IV TR emissions are fainter or not visible in the RE locations. The fact that there is little or no Fe XXI evaporation is in agreement with what is shown in Figure 7 of Panos & Kleint (2021). In this figure the authors show that the most probable spectra (red) associated with the RE profiles (top panels) do not contain clear Fe XXI emission, or even when they do (less probable spectra in blue), the line is often not significantly blueshifted, or in other words there is no clear chromospheric evaporation simultaneous with RE profiles. On the other hand, the evaporation is stronger in the bright ribbon part (middle and bottom panels of that figure). As also mentioned in Panos & Kleint (2021), in principle this could be due to a delay in the formation of the Fe XXI line. The FL3 sit-and-stare observation we analyze here is best suited to investigate the time delay between the appearance of the RE profiles and evaporation, thanks to higher cadence (around 9 s). Panels (c) and (d) of Figure 4 show that the "southern" branch of the single ribbon observed under the IRIS slit shows a number of pixels where the RE Mg II profiles have been identified, but no Fe XXI emission or evaporation is visible there at any later time. We note that this might be partly caused by the high inclination of the flare loops. For the few pixels in the "upper" branch where do we see evaporation at a later time (green contours in panels (b) and (c)), we calculated an average delay of 45 s between the appearance of the RE profiles and the Fe XXI evaporation.

Finally, we summarize the observational parameters of the RE Mg II profiles for FL1–FL4 in Figures 6 and 7 and Table 1, as will be discussed in the following sections.

3. Forward Modeling of IRIS Flare Emission

In this section we describe the method we use to simulate the IRIS synthetic spectra using a grid of `RADYN+FP` simulations (Section 3.1). We post-process `RADYN+FP` atmospheres through the `RH15D` code for the synthesis of the Mg II emission (Section 3.2) and the CHIANTI v.10 (Dere et al. 1997; Del Zanna et al. 2021) atomic database for the optically thin emission (Section 3.3). The synthetic spectra and parameters that we obtain from the simulations are shown in Figures 6, 7, and 8 and in Figures 11–14 in the Appendix, summarized in Table 1 and finally discussed in detail in Section 4.

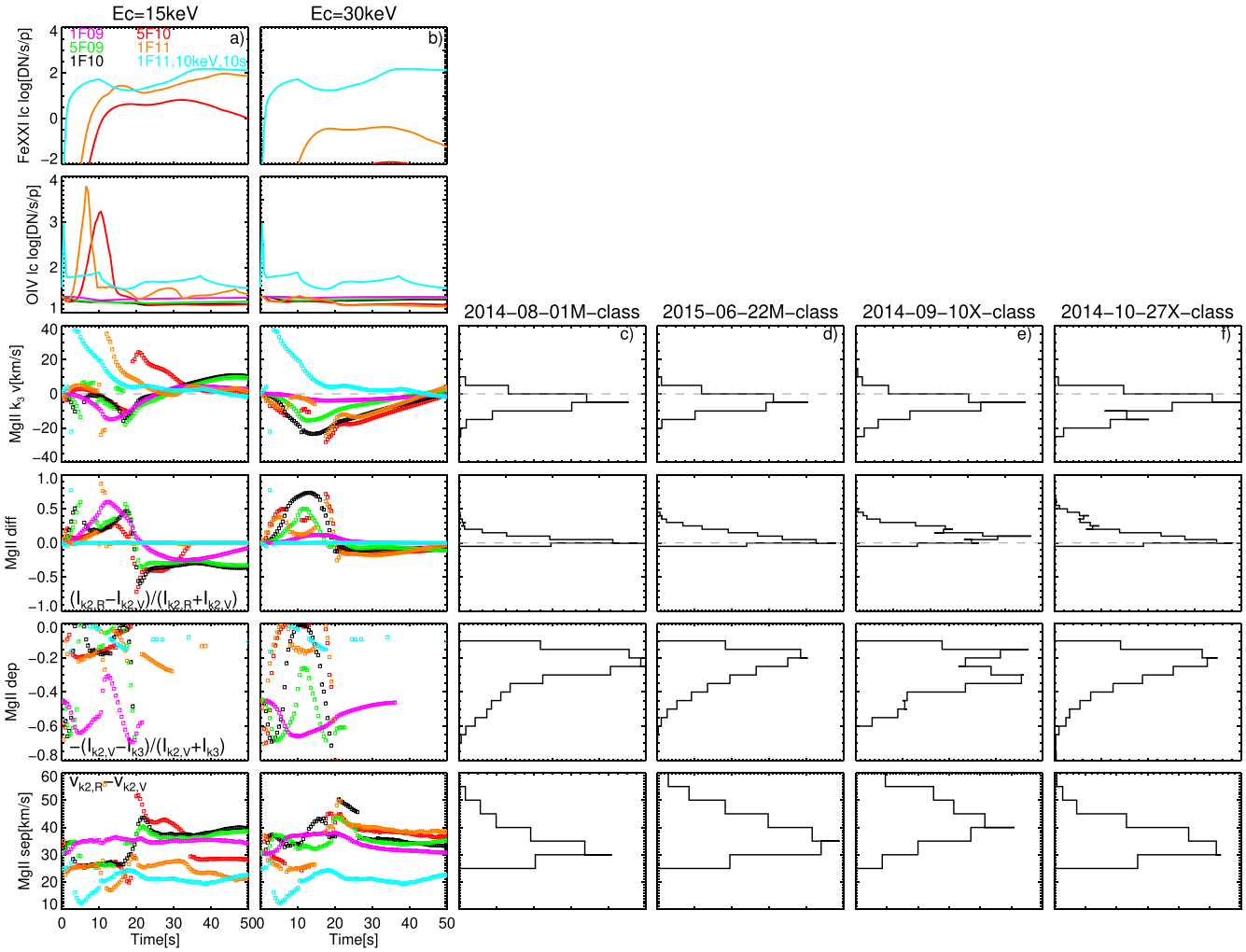

Figure 6. (a–b) Summary of parameters from RADYN+FP+RH15D simulations assuming *gradual* heating over 20 s as a function of time. Gaps in the synthetic curves shown with squares indicate time steps in the simulations where the line goes single peaked, where the line goes triple peaked, or where the fit fails. (c–f) Comparison with histograms of observed RE metrics for FL1–FL4.

3.1. RADYN Simulations

To investigate the origin of the enhanced absorption of the He I λ10830 line at the flare leading edge, Kerr et al. (2021) produced a large grid of flare simulations using the RADYN RHD model (Carlsson & Stein 1995; Allred et al. 2005, 2015), which uses the nonthermal particle transport code FP (Allred et al. 2020) to propagate a distribution of nonthermal particles through a flare loop. We use a subset of those simulations here, synthesizing from them the Mg II NUV spectra, as well as Fe XXI and O IV emission. For full details of these RADYN+FP simulations and the code in general, consult Kerr et al. (2021).

The simulations selected for use here covered a wide range of energy fluxes, with energy deposition via an injected distribution of nonthermal electrons. The fluence (time-integrated energy flux) was varied, with $F = [1 \times 10^{10}, 5 \times 10^{10}, 1 \times 10^{11}, 5 \times 10^{11}, 1 \times 10^{12}]$ erg cm^{-2}. These electron beams were injected for either $t_{\rm inj} = 10$ s (a constant flux) or $t_{\rm inj} = 20$ s (a triangular profile with a peak at 10 s), the latter to investigate a more gradual injection. In the remainder of the text we refer to the instantaneous energy flux (erg cm^{-2} s^{-1}) alongside the injection time, as this property is more commonly used in the flare literature, where for the $t_{\rm inj} = 20$ s cases we quote the peak instantaneous energy flux. The spectral shape of those distributions was varied also. The spectral index $\delta = 5$ was fixed, but two values of the distribution's low-energy cutoff were studied, $E_c = [15, 30]$ keV, allowing us to study the difference between a "softer" and "harder" nonthermal electron spectrum. The latter contains a larger proportion of higher-energy electrons, capable of penetrating more deeply and resulting in a smaller amount of heating of the upper chromosphere/lower TR. This was motivated because Kerr et al. (2021) found that a harder distribution, with a weaker energy flux, resulted in stronger, slightly longer-lived periods of enhanced absorption of the He I λ10830 line (i.e., those simulations were more consistent with the ribbon front observation of Xu et al. 2016). We now ask, do the synthetic Mg II line profiles for those same simulations similarly appear more consistent with the observed ribbon front profiles?

For comparison, we also analyze a flare simulation that is more efficient at heating the TR and driving chromospheric evaporation, that is, a simulation with a large impulsive energy flux (10^{11} erg cm^{-2} s^{-1} with constant $t_{\rm inj} = 10$ s), low-energy cutoff ($E_c = 10$ keV), and $\delta = 5$.

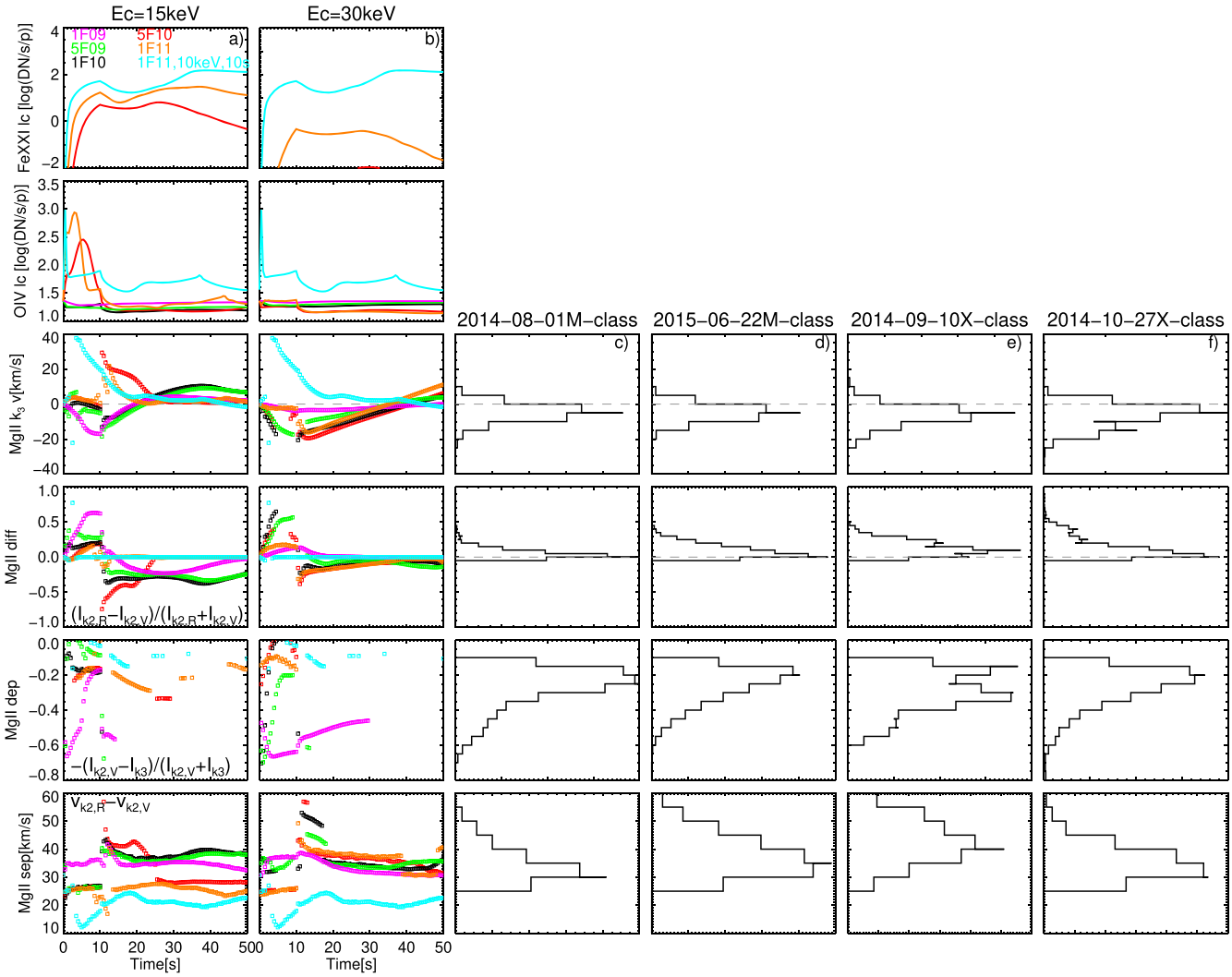

Figure 7. Same as Figure 6, but for models with constant 10 s heating.

3.2. *Synthesis of Mg II Emission*

To synthesize the Mg II NUV spectra from our RADYN+FP simulations, we used the radiation transport code RH15D (Uitenbroek 2001), which solves the equation of radiation transport and atomic level populations given an input atmosphere. Flare atmospheres (temperature, electron density, bulk velocity, hydrogen atomic level populations) were input to RH15D, with a cadence of 0.5 s. The non-LTE radiation transport was solved for H, Mg II, and Ca II, with 15 additional species solved in LTE as sources of background opacity. An additional source of line broadening due to microturbulence was included, with a constant value of 7 km s^{-1} (consistent with Carlsson et al. 2015). This value is consistent with a recent study by Sainz Dalda & De Pontieu (2022), who found microturbulence velocities between 5 and 15 km s^{-1}, based on inversions of IRIS Mg II profiles during flares. The atmosphere above a temperature of 30 kK was discarded in the solution to reduce computational time.

When solving the Mg II radiation transfer, we used the 10-level-plus-continuum model atom from Leenaarts et al. (2013a) and included the effects of partial frequency redistribution via the hybrid scheme of Leenaarts et al. (2012), which has been shown to be required both in quiet Sun and in flares (Leenaarts et al. 2013a; Kerr et al. 2019a). While RADYN+FP includes nonequilibrium ionization, RH15D does not, solving each time step in isolation assuming statistical equilibrium. This is somewhat mitigated by using the nonequilibrium electron density from RADYN+FP, but it was also demonstrated that the assumption of statistical equilibrium is largely sufficient for Mg II even in flares (Kerr et al. 2019b).

The synthetic Mg II NUV spectra were converted to the IRIS count rates by (1) convolution with a spectral point-spread function assumed to be a Gaussian with FWHM of 52 mA (two IRIS spectral pixels), (2) recasting to the IRIS spectral plate scale (26 mA) and multiplying by the spectral dispersion, (3) converting intensity from erg to photons, (4) multiplying by the solid angle subtended by an IRIS SG pixel, (5) multiplying by the IRIS effective area, and (6) converting from photons s^{-1} to DN s^{-1} (18 photons DN^{-1} in the NUV; De Pontieu et al. 2014). An exposure time of 1 s was assumed. Finally, the same metrics as calculated for the observations were calculated from these synthetic IRIS spectra (see Section 2.1).

In the Appendix, we show the synthetic spectra of Mg II and Mg II triplet as a function of time for the subset of the models from Kerr et al. (2021) that we analyze here.

Table 1
Spectral Characteristics of IRIS Lines for Different RADYN+FP Models

Model			IRIS Spectral Features					
F (erg cm^{-2} s^{-1})	E_C (keV)	τ_H (s)	Fe XXI em[a]	O IV em[b]	$\nu_{O\ IV}$ (km s^{-1})[c]	DCR[d]	ν_{CR} (km s^{-1})[e]	tDCR[f]
10^9	15	20(t)	No	No	Blue	Yes	Blue	No
10^9	30	20(t)	No	No	Blue wing	Yes	Blue	Yes
5×10^9	15	20(t)	No	No	Blue	No	Blue	No
5×10^9	30	20(t)	No	No	Blue	Yes	Blue	Yes
10^{10}	15	20(t)	No	No	Blue	No	Blue	No
10^{10}	30	20(t)	No	No	Blue	Yes	Blue	Yes
5×10^{10}	15	20(t)	Yes	Yes	Blue	No	Blue	No
5×10^{10}	30	20(t)	No	No	Blue	No	Blue	No
10^{11}	15	20(t)	Yes	Yes	Blue/Red(blue followed by red)	No	Red	No
10^{11}	30	20(t)	No	No	Blue	Yes	Blue	No
10^9	15	10(c)	No	No	Blue	Yes	Blue	No
10^9	30	10(c)	No	No	Blue	Yes	Blue	Yes
5×10^9	15	10(c)	No	No	Blue	No	Blue	No
5×10^9	30	10(c)	No	No	Blue	No	Blue	No
10^{10}	15	10(c)	Yes	Yes	Blue	No	Red	No
10^{10}	30	10(c)	No	No	Blue	No	Blue	No
5×10^{10}	15	10(c)	Yes	Yes	Blue/Red	Yes	Red	No
5×10^{10}	30	10(c)	No	No	Blue	Yes	Blue	No
10^{11}	15	10(c)	Yes	Yes	Blue/Red	Yes	Red	No
10^{11}	30	10(c)	No	No	Blue	Yes	Blue	No
10^{11}[f]	10	10(c)	Yes	Yes	Red	No	Red	No
Observation of RE profiles			No	No	Blue/Red[g]	Yes	Blue	Yes/No

Notes.
[a] Significant Fe XXI emission.
[b] Increased O IV emission.
[c] "Deep" central reversal in Mg II k3.
[d] Doppler shift of Mg II k3 central reversal in km s^{-1}.
[e] "Deep" central reversal in Mg II triplet.
[f] "Evaporation" simulation.
[g] See Section 4.3.

3.3. Synthesis of Optically thin Fe XXI and O IV Emission

Similarly to what was done in our previous work (Polito et al. 2018, 2019), we synthesize the emission of the optically thin Fe XXI and O IV lines using the values of density, temperature, and bulk velocity at each grid point and time step from the RADYN+FP simulations and atomic data from CHIANTI v.10 (Dere et al. 1997; Del Zanna et al. 2021) assuming photospheric abundances (Asplund et al. 2009). In particular, we follow Equation (1) of Polito et al. (2018) and convert the synthetic spectra in units of DN s^{-1} pixel^{-1} assuming the IRIS unsummed spatial pixel dimension (e.g., 0.″33–0.″166), a spectral bin of 0.026 Å, and a gain of 4 photons DN^{-1} for the FUV channel (De Pontieu et al. 2014). The time–velocity spectra in Figure 8 are then obtained by integrating the synthetic emission in each RADYN+FP grid point along the loop as a function of time, and they are plotted every 1 s. Finally, we take into account the IRIS instrumental broadening of 0.026 Å when synthesizing the line emission.

4. Discussion

4.1. Model–Data Comparisons

In Figures 6 and 7 we compare the observational results from IRIS with the predictions from the RADYN+FP and RH15D models, with gradual and constant heating profiles, respectively. For each figure, the first two columns from the left show the model predictions for models with E_C of 15 and 30 keV, respectively. From top to bottom, we plot the Fe XXI and O IV intensities, Mg II k3 line core velocity, peak difference, depth of central reversal, and peak separation as a function of time. To calculate and define the Mg II spectral parameters, we have used the same method and definitions (e.g., Equations (1)–(3)) as those used in Section 2 for the observations. The third to sixth columns in Figures 6 and 7 show histograms of the same Mg II parameters that we have obtained for the four flare observations described in Section 2. We note that we do not report the values of Fe XXI and O IV intensities for the observations since these lines are often not observed or very faint in the same pixels where we see the RE profiles. In addition to the RADYN+FP models presented in Kerr et al. (2021), the synthetic parameters for a more "typical" flare simulation that is efficient at driving evaporation (see Section 3.1) are also shown in light blue in Figures 6 and 7.

Table 1 also summarizes the quantitative behavior of the IRIS spectral lines in the models analyzed here, as well as the observations. The entries in the observational row are taken from the analysis of the data sets presented here, which are also consistent qualitatively with Panos et al. (2018, 2021).

Below we summarize the main findings from our model–data comparison based on Figures 6 and 7 and Table 1:

1. The "typical" flare simulation with large impulsive flux (10^{11} erg cm^{-2} s^{-1} with constant $t_{\rm inj}=10$ s) and $E_c=10$ keV produces the strongest Fe XXI and TR emission. This is not surprising since the strong energy flux with a softer low-energy cutoff means that most of the energy is deposited in the TR, where it quickly drives

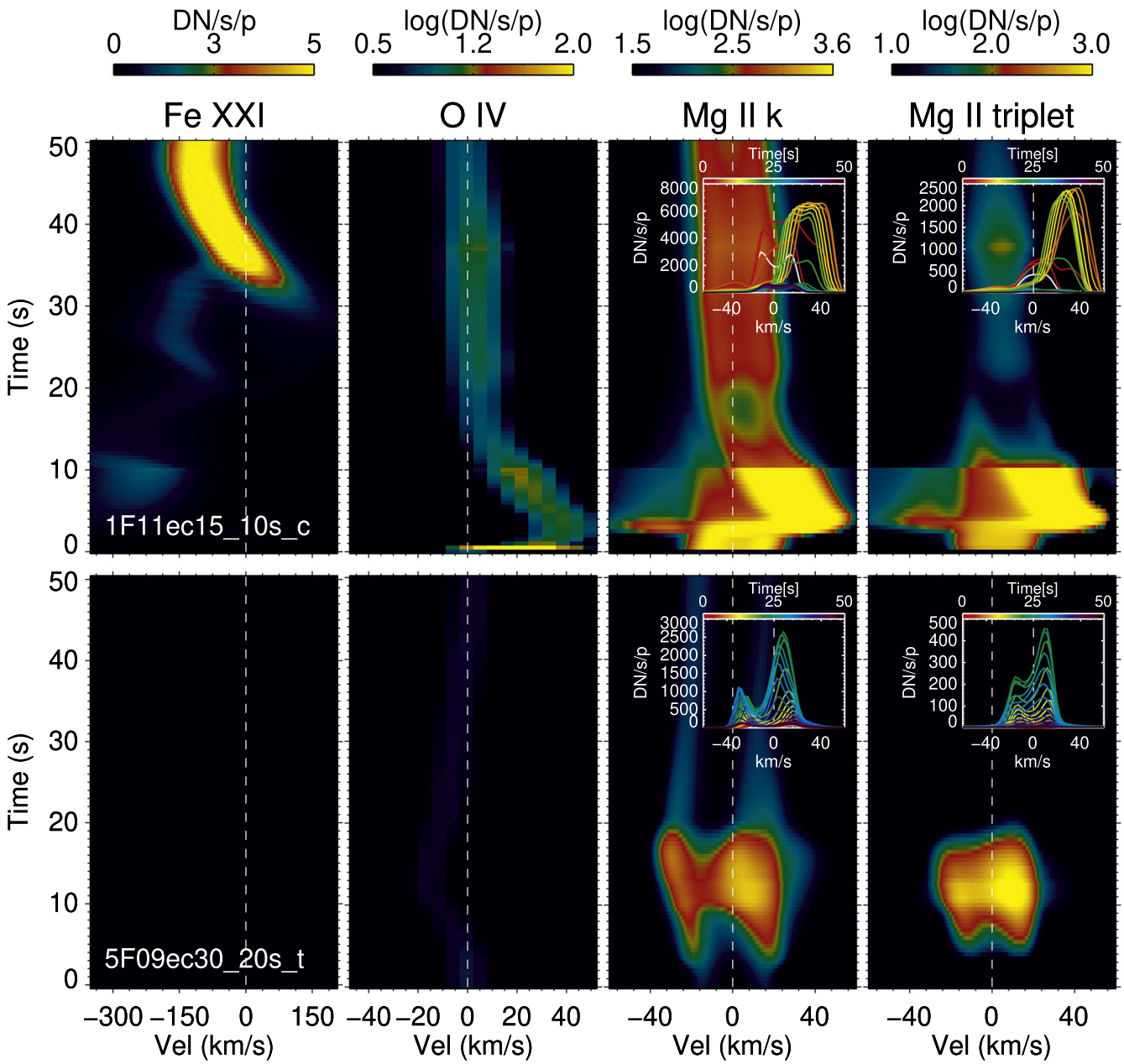

Figure 8. From left to right: Fe XXI, O IV, and Mg II *k* and triplet synthetic spectra for a "typical" evaporation model (top) and a model that we suggest reproduces quantitatively the ribbon leading edge behaviors (bottom). The insets in the Mg II *k* and triplet spectra show the evolution of the synthetic spectra over 4 s. For a summary of all the models results, see Table 1 and Figures 11–14 in the Appendix.

the plasma to million-degree temperatures where Fe XXI is formed. When the plasma is not able to radiate the energy away, the overpressure will drive the chromospheric evaporation (e.g., Fisher et al. 1985). However, the same simulation does not seem to reproduce the more typical properties of the RE profiles. In particular, the synthetic profiles show that the cores of the Mg II lines are mostly redshifted, with shallow central reversal and small peak separation.

2. Most of the electron beam models above (from Kerr et al. 2021), apart from the "evaporation" model (light-blue curves), can reproduce, even if just for a short time, asymmetric profiles with stronger red peak and slightly blueshifted line core, consistent with IRIS observations. In addition, the range of blueshifts for the line core seems to reproduce the magnitude of those seen in the observations. The values of peak separation in the models from Kerr et al. (2021) also reproduce the observed values. This might be due to the fact that we added a microturbulence of $7\,\mathrm{km\,s^{-1}}$ in the `RH15D` models, following Polito et al. (2018) and Carlsson et al. (2015).
3. The spectral parameter that best distinguishes the models is the depth of the central reversal. We emphasize that in the observations we have made no distinction between the two types of "weak" and "strong" ribbon profiles of Panos et al. (2021) and that the strong tails of deeper central reversal values in the histograms of Figures 6 and 7 are more representative of the strongest profiles with deeper reversal. For the gradual heating models (Figure 6), the simulations that reproduce the strongest

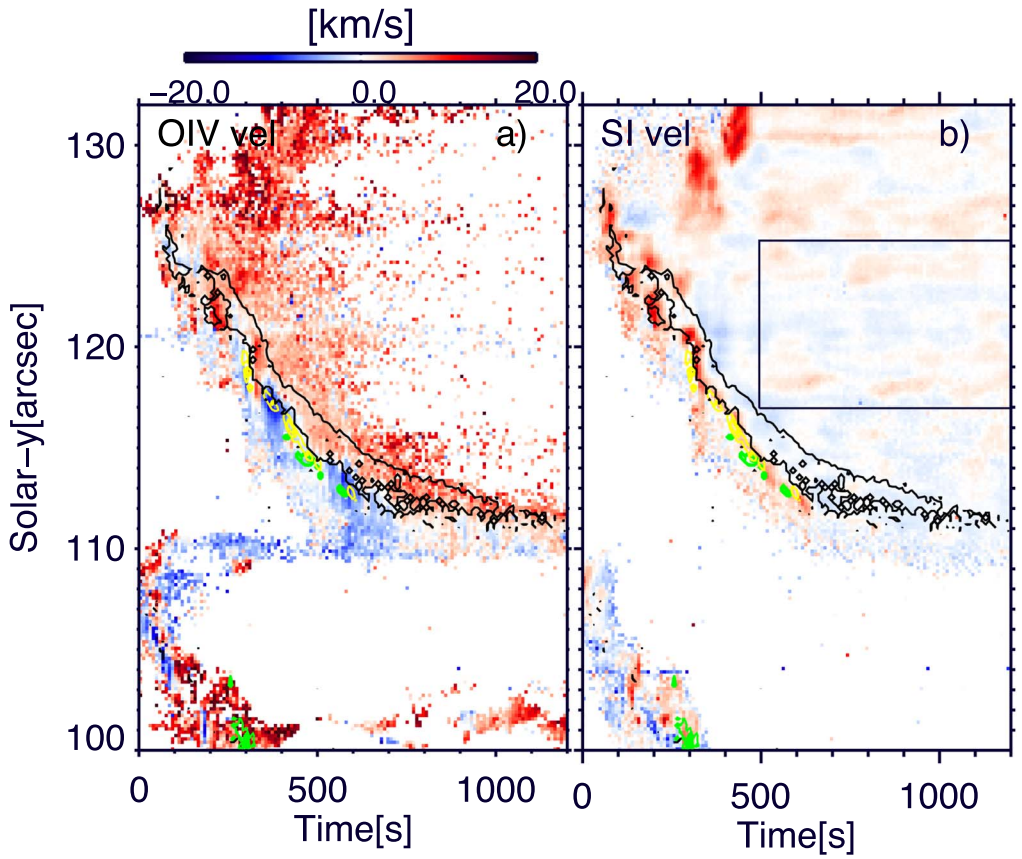

Figure 9. Doppler shift maps (spatial position along the slit vs. time) of O IV and S I around 1401 Å for flare FL3. The green, yellow, and black contours show the location of the ribbon leading edge pixels, the maximum O IV intensity, and the maximum Fe XXI evaporation, respectively. The box in the S I map shows the area where we measured the average Doppler shift to verify wavelength calibration. See text for more details.

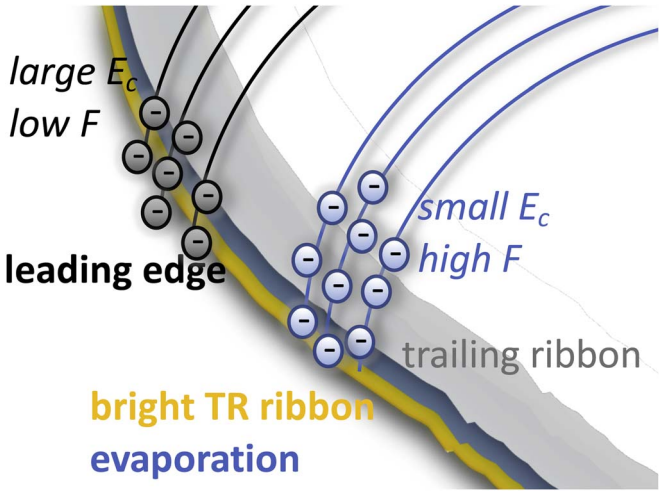

Figure 10. Cartoon illustrating our proposed scenario where two distinct physical mechanisms are responsible for heating the leading edge of the ribbon and the bright part where strong TR emission and evaporation are observed. Based on the analysis of FL3, we also show that there is a small shift between the locations of maximum TR ribbon intensity and the evaporation.

central reversals in Mg II are those with the more modest energy fluxes of 1–5F9 (magenta color) for the smaller E_C (first column). However, even gradual heating models with higher energies fluxes up to 1F11 can to some extent explain the deep central reversals if the E_C is larger (30 keV). For a fixed flux, electron beams with stronger E_C contain a larger fraction of high-energy electrons, capable of penetrating deeper into the atmosphere in the formation region of the line peaks. There the beam heating will drive an increase in the plasma density that causes the stronger reversal of the line core compared to the peaks.

4. The constant heating models are less successful at explaining the strongest deep central reversals. In particular, the ones that work best are again the ones with more modest (1–5F09) energy flux and larger E_C. For the smaller E_C of 15 keV (softer beams) only the 1F09 model can explain the very large central reversals of the "strong" ribbon front profiles.
5. The simulations that can reproduce a deep central reversal for the longest time are the gradual heating simulations with 1–5F9 with $E_C = 30$ keV, the 1F9 simulation with $E_C = 15$ keV, and the 1F9 constant heating simulation with $E_C = 30$ keV. However, the 1F9 simulations deposit very little energy in the atmosphere and produce faint line emission for both the Mg II and Mg II triplet. In the observations the Mg II line is often observed to be fainter at the ribbon front profiles (see Figures 2–5), and also the Mg II triplet emission can vary based on the observation.

In addition to what is discussed above, in Table 1 we also add the information regarding the TR Doppler shift for all models. One thing that seems to be discrepant between models and observations in some cases is the Doppler shift of the TR lines. This topic is discussed separately in Section 4.3.

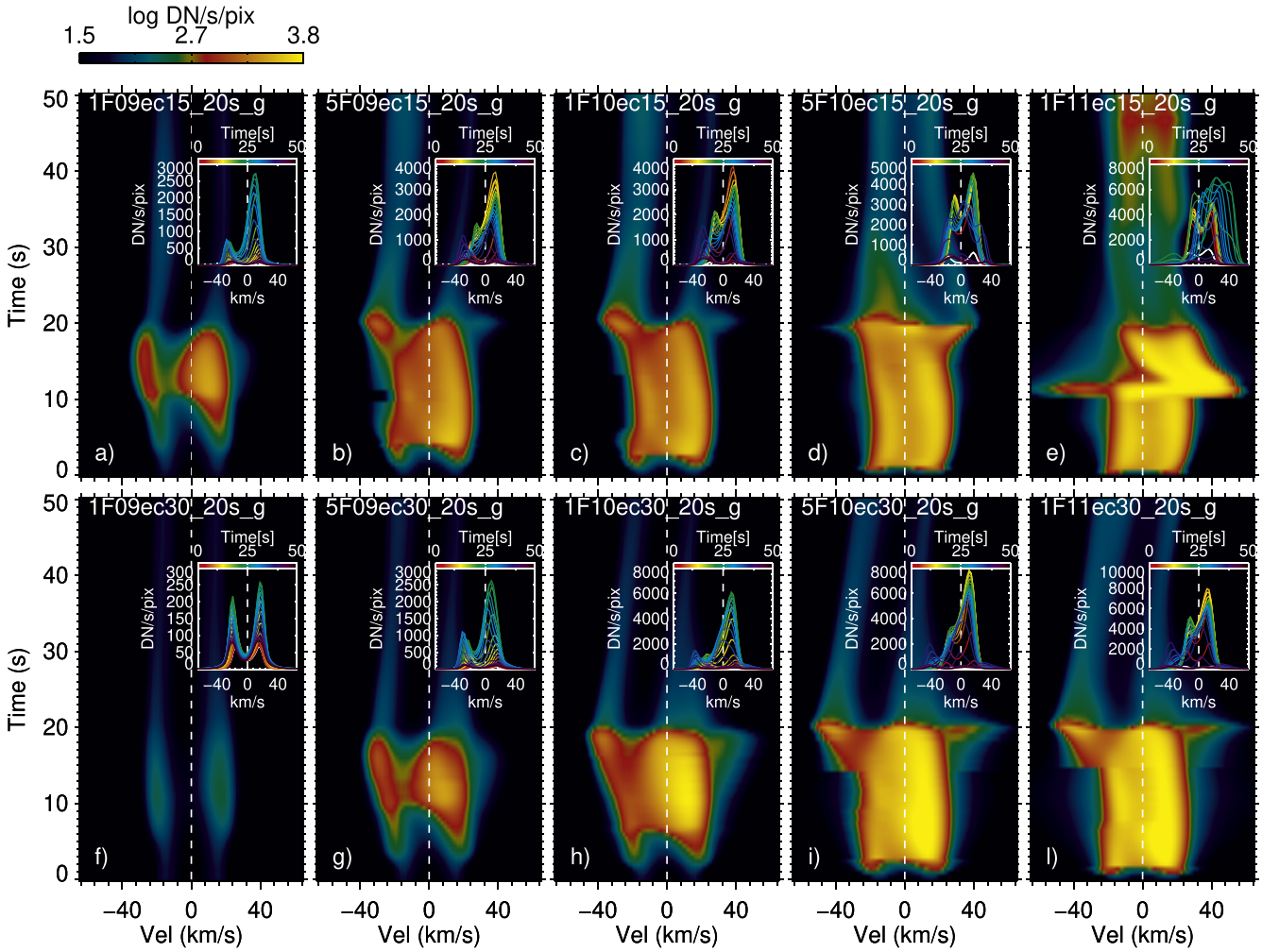

Figure 11. Mg II k spectra for gradual heating models.

To summarize, the model–data comparison above seems to suggest that we need two types of substantially different models to explain the behavior of the main bright ribbon, where the evaporation is observed, and the "leading edge" of the ribbon, where the typical profiles identified by Xu et al. (2016) and the series of papers by Panos et al. are found.

In Figure 8 we show the synthetic spectra over time for Fe XXI, O IV, Mg II k, and Mg II triplet for a more "typical evaporation" simulation (top panels), which we speculate could be representative of the heating mechanism for the main bright ribbon, and one of the gradual heating simulations that best reproduces quantitatively the behavior of the ribbon front profiles observed with IRIS (bottom panel). We also note that this type of simulation (gradual and modest energy release and harder beam) can also reproduce the increased absorption in He I λ10830 that has been observed by Xu et al. (2016), as shown in Kerr et al. (2021).

However, it is important to note that while the "typical evaporation" simulation produces Mg II h and k lines with much shallower reversals, it still cannot reproduce the single-peaked behavior of the Mg II line typically seen in the main bright ribbon. This is a common problem that has been discussed by several authors, which seems to be the result of an underestimation of electron density in the upper chromosphere (e.g., Rubio da Costa & Kleint 2017; Zhu et al. 2019).

As mentioned in Section 2, in our FL2 observation we see a delay of about 45 s between the appearance of the RE profiles and the Fe XXI evaporation. In addition, Panos et al. (2021) state that on average it takes about 1–3 minutes for the RE profiles to become single peaked. Since our loops are heated for 20 s, one might wonder whether extending the duration of the heating in one of the simulations that reproduces the ribbon front profiles might naturally lead to Fe XXI evaporation. While we are working on a follow-up paper focused on the long duration of the ribbon front profiles (Kerr et al. 2023, in preparation), we have also performed preliminary experiments to explore this possibility, as discussed below (Section 4.2).

4.2. Do We Need Different Models for Heating the Main Bright Ribbon and the Leading Edge?

Based on the comparison between models and observations presented above, we speculate that we need different types of electron beam models to explain heating in different parts of the ribbons at a certain time, namely the "leading edge" and the main bright ribbon. However, since in some cases the same location where we see the ribbon front profiles later can show the typical features of the bright ribbon (i.e., Fe XXI evaporation, increased TR emission, and single-peaked Mg II profiles), an alternative explanation could be that the same heating models that initially reproduce the ribbon front

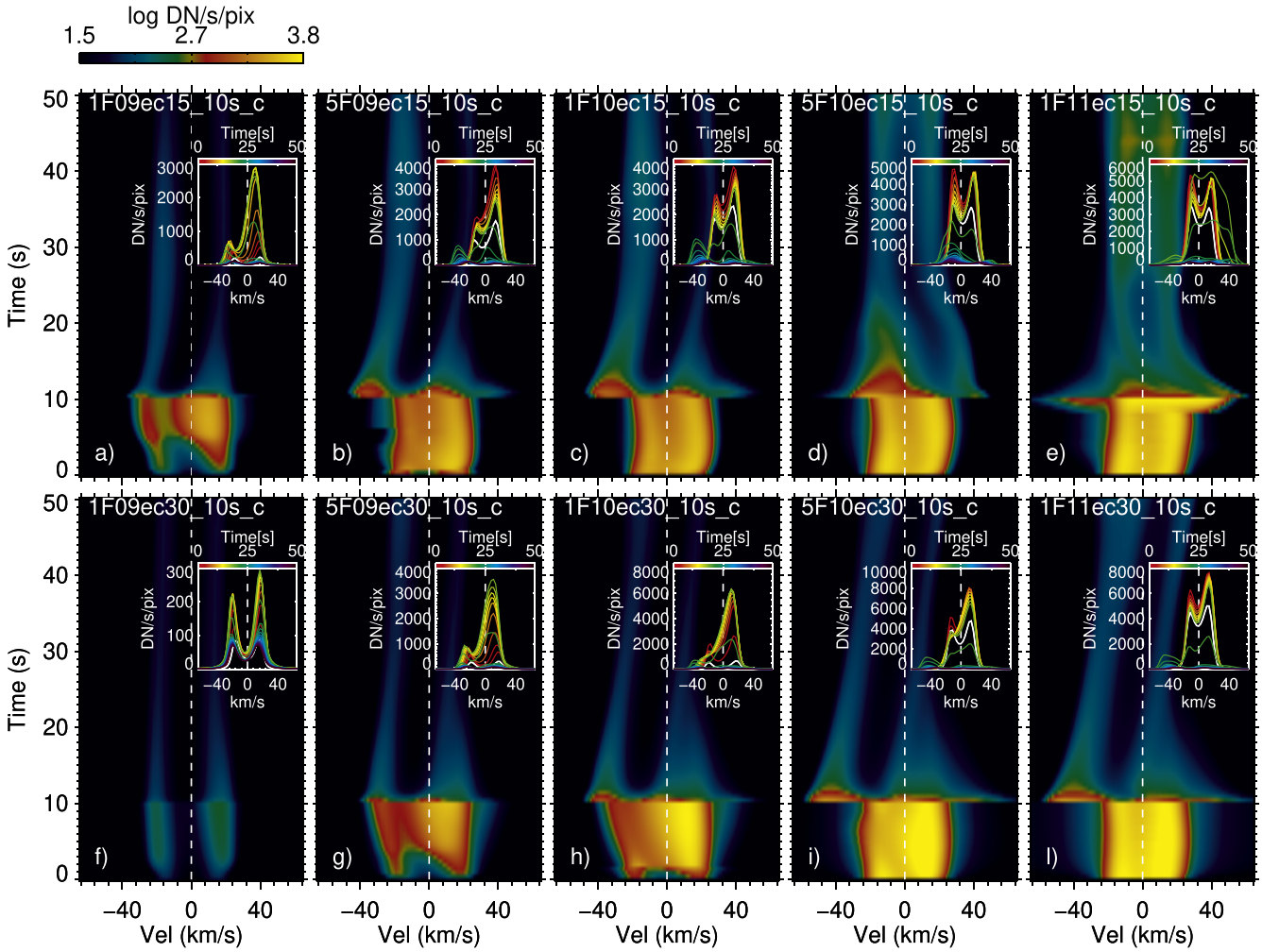

Figure 12. Mg II k spectra for constant heating models.

profiles then naturally also produce these typical features. Since the delay between the two regimes of behaviors can be a few tens of seconds as discussed above, the simulations from Kerr et al. (2021) that we have discussed so far cannot directly answer this question since they are assuming a heating duration of up to 20 s and the total duration of the simulations is 50 s. To address this issue, we ran some additional RADYN+FP simulations where we used the same electron beam parameters as in the model that we have chosen to be representative of a "ribbon front-type" of heating (Figure 8, bottom panels) but with longer duration, as summarized below:

1. A model with a gradual triangle heating profile with peak energy flux of 1.67×10^9 erg cm^{-2} s^{-1} (1.67F09), $E_C = 30$ keV, and $\delta = 5$, where the heating is released over 60 s instead of 20 s. The total energy integrated over time will be the same as that of the 5F09 simulation with $E_C = 30$ keV and $\delta = 5$ that we have described in the previous sections.
2. A model with a gradual triangle heating profile with peak energy flux of 5×10^9 erg cm^{-2} s^{-1} (5F09), $E_C = 30$ keV, and $\delta = 5$, where, however, the heating is released over 60 s instead of 20 s. The total energy integrated over time will be higher than the 5F09 simulation with $E_C = 30$ keV and $\delta = 5$ that we have described in the previous sections.
3. A model with a gradual rising phase that is the same as the 5F09 simulation with $E_C = 30$ keV that is shown in Figure 8 (i.e., that reaches a peak energy flux of 5×10^9 erg cm^{-2} s^{-1} at $t = 10$ s), but it then stays constant for a further 110 s.

We also let the three simulations evolve until they reach 120 s. These simulations all reproduce He I λ10830 enhanced absorption followed by emission (not shown here). In Figure 15 in the Appendix we show the synthetic spectra of the Fe XXI, O IV, Mg II, and Mg II triplet lines for the additional models described above. The spectral characteristics of the Mg II k and triplet lines are similar to those observed in the bottom panels of Figure 8, but the longer heating duration does not naturally lead to Fe XXI evaporation and increased TR emission as more typically observed in the main bright ribbon. We also emphasize that the simulation that produces the latter behavior (e.g., top panels of Figure 8) does not reproduce the ribbon front typical profiles before the onset of the evaporation either. We then conclude that the heating models that drive these two different regimes must be different, or that the electron beam parameters change over time. One other point that was also discussed in Kerr et al. (2021) is that both the enhanced absorption of He I λ10830 and the Mg II ribbon front profiles (e.g., Panos et al. 2021) can be sometimes observed for a few minutes, while our models can reproduce these behaviors

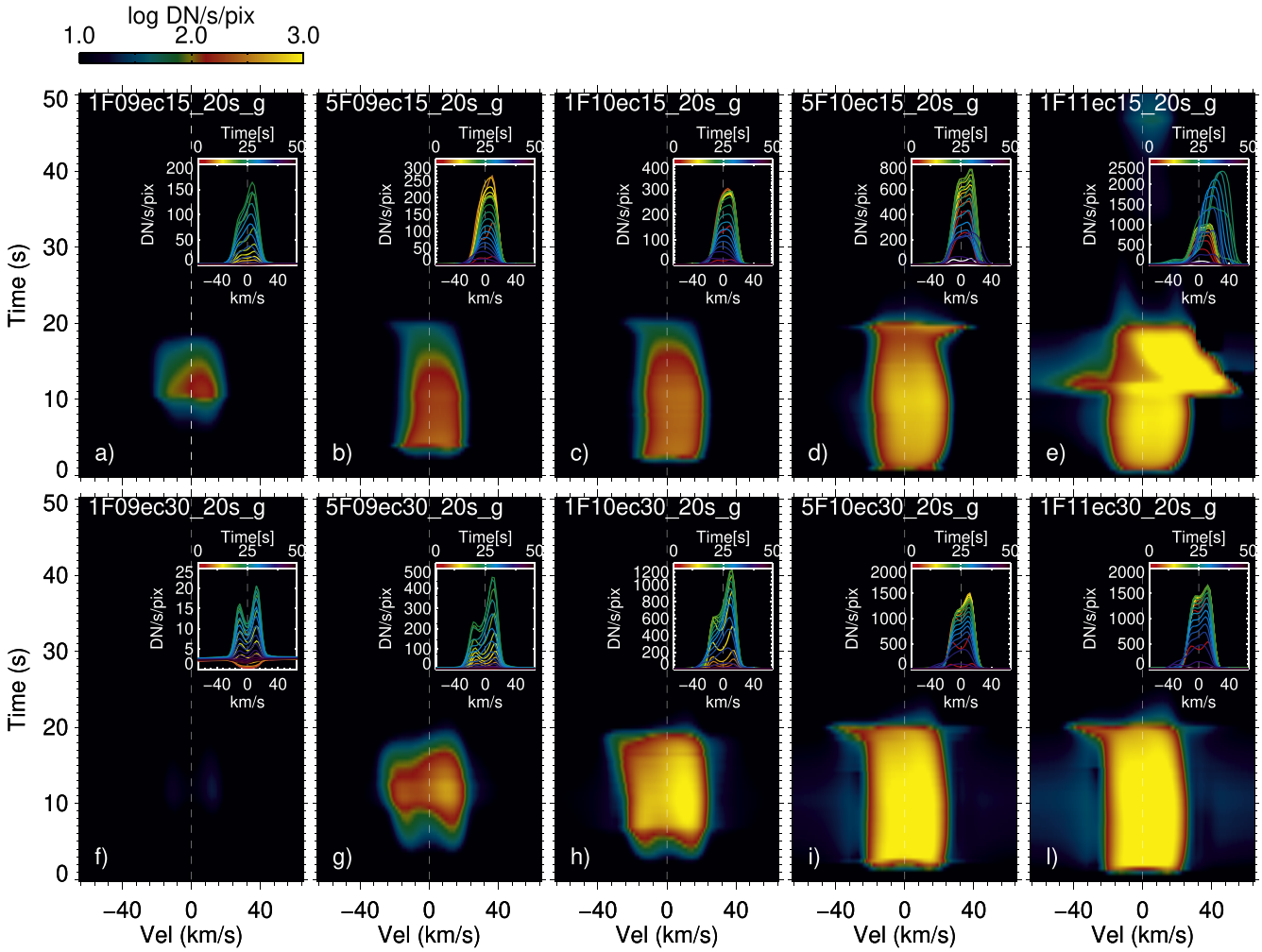

Figure 13. Mg II triplet spectra for gradual heating models.

for a period closer to a few seconds at most. A follow-up work focused on the long-term evolution of the ribbon front profiles is currently under preparation (Kerr et al. 2023, in preparation).

4.3. Transition Region Emission

Flare ribbon observations most commonly show that the TR emission is redshifted in the ribbon area (e.g., Tian et al. 2015; Polito et al. 2016; Reep et al. 2018a), with some exceptions (e.g., Jeffrey et al. 2018; Lörinčík et al. 2022). Nevertheless, not many authors so far have focused on the local differences in the TR spectra between the main bright ribbon and the leading edge locations. We analyzed in detail the O IV spectra in the ribbon front region for two of the four flares under study (see Figures 9 and 16) and found that the line appears to be blueshifted at least in some locations within the ribbon fronts.

Figure 9 shows Doppler shift maps of the O IV and S I line for FL3 as obtained by performing a single Gaussian fit in each IRIS pixel. The IRIS level 2 data are corrected for the orbital drift of the wavelength array. However, in order to perform an absolute wavelength calibration, it is usually recommended to measure the wavelength position of one of the photospheric lines included in the IRIS spectra in case a small residual drift is still present. The closest photospheric line to the O IV lines is the S I line around 1401 Å. To verify the wavelength calibration, we took the average wavelength of the S I line in a region along the flare loops during the gradual phase and obtained a velocity of ≈ 0 km s^{-1}, as expected if the wavelength calibration is correct. Note that the line is too faint to be observed reliably outside the flare.

The green, yellow, and black contours in the figure show the location of the ribbon leading edge pixels, the maximum O IV intensity, and the maximum Fe XXI evaporation, respectively. The O IV Doppler map thus shows that in the ribbon leading edge the line is fainter (but still reliably measurable as we verified while performing the fit) and blueshifted. The line is instead redshifted in the main bright ribbon where the evaporation (black contours) is observed. We also note that there is a small shift between the region of maximum TR line intensity (yellow contours) and FUV continuum (not shown here) and evaporation (black contours). An offset of about 0.″5–1″ between the location of maximum Fe XXI evaporation and the ribbon site had been reported before by, e.g., Young et al. (2015), who suggested that this offset might occur if the evaporation increases after the initial burst of chromospheric heating that causes the chromospheric ribbon.

Similarly, Figure 16 shows the O IV Doppler shifts for two example rasters during FL2 (a movie is also available). Since the signal for this flare was sometimes small given the short exposure time (∼1 s), we binned the data by an additional factor of 2 in the *Y*-direction. The figure and corresponding movie suggest that the O IV Doppler shift is sometimes

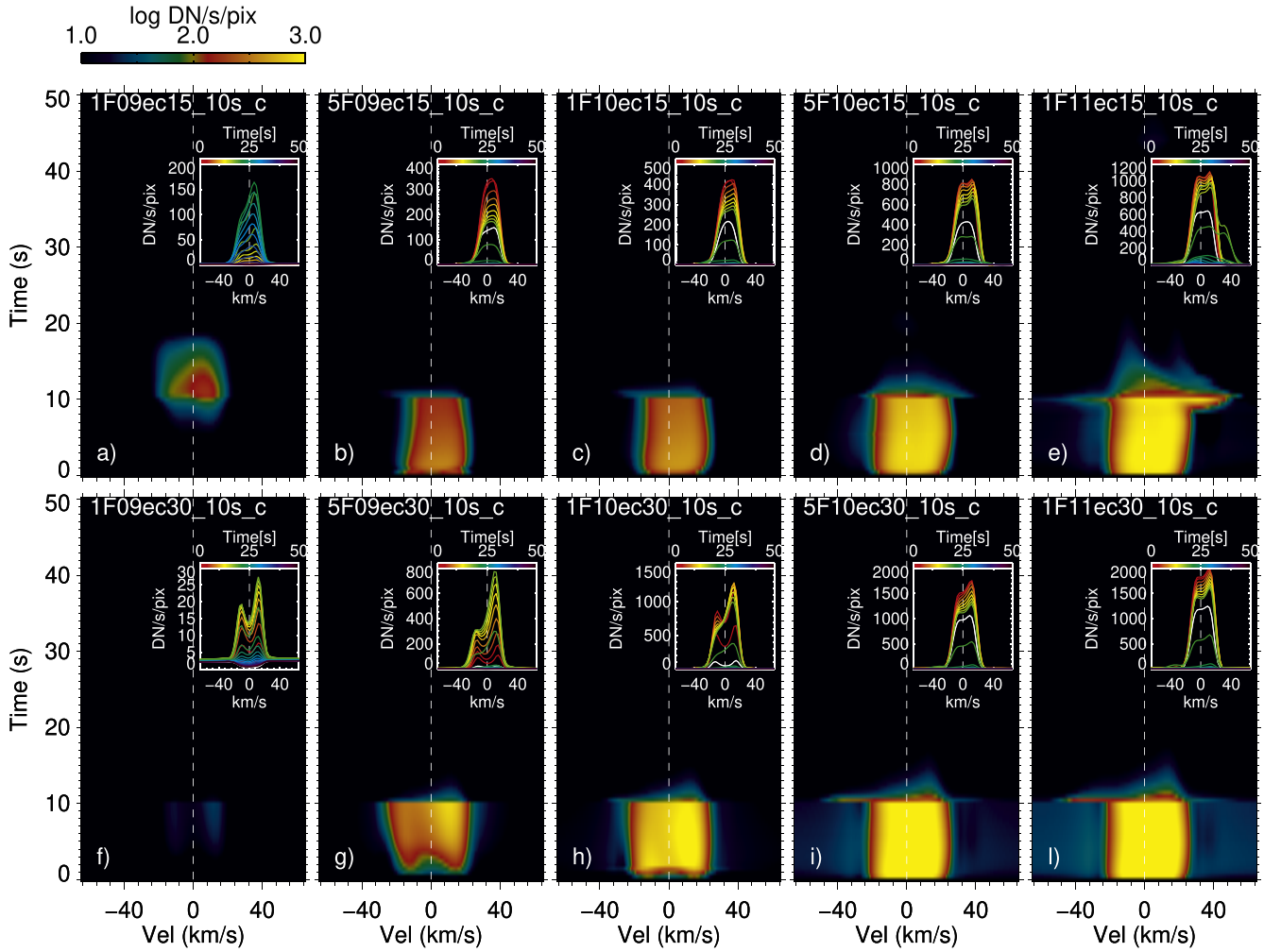

Figure 14. Mg II triplet spectra for constant heating models.

blueshifted and other times redshifted in the location of the ribbon front profiles.

We also note that Panos & Kleint (2021) showed the characteristics Si IV profiles in the ribbon front location in Figure 7 of their paper. According to their figure, in some cases the TR line exhibits a blueshift or a blue wing in the ribbon front profiles (blue curves), although the most likely profiles (red curves) are redshifted. However, the profiles also often exhibit spectral characteristics, including absorption features, which are typical of optically thick conditions (see, e.g., the profiles in the top left multipanel in their figure). We suggest that a future statistical study using ML on the O IV λ1401 instead of the Si IV lines (for observations where the O IV line is visible enough) might provide useful insights into the behavior of the TR in the ribbon leading edge and thus crucial constraints on the models. Being intercombination lines with a very small A-value, the O IV lines are in fact optically thin (e.g., Appendix A of Doschek & Feldman 1978; Dudík et al. 2017).

Based on our preliminary results, we conclude that the optically thin TR lines such as O IV *can* be blueshifted in the ribbon front profiles, in agreement with our speculation based on the `RADYN+FP` models.

It is also possible that the regional signatures that characterize the ribbon front in the TR lines are not as clear as those observed in the chromospheric lines, and that the TR lines there can be both blueshifted and redshifted.

On the other hand, since we can already explain the cases when the O IV lines are blueshifted, we investigated whether we can reproduce *redshifted* TR emission for our gradual gentle heating models by adding in situ heating in the corona. Previous work (e.g., Testa et al. 2014; Polito et al. 2018) has in fact shown that in situ typically produces downflows in the TR.

To model the effects of in situ energy deposition and the subsequent conductive heat flux through the corona to the TR and chromosphere, we experimented with adding an additional ad hoc volumetric heating rate to the loop top in the $F_{\rm peak} = 5 \times 10^9$ erg s^{-1} cm^{-2}, $\delta = 5$, $E_c = 30$ keV, $t_{\rm inj} = 20$ s electron beam simulation. These volumetric heating rates were $Q_{\rm adhoc} = [1.0, 2.5, 5.0, 7.5, 10]$ erg s^{-1} cm^{-3}, applied for 10 s over the top 200 km of the loop (giving instantaneous energy fluxes of $F_{\rm adhoc} = [0.2, 0.5, 1.0, 1.5, 2.0] \times 10^9$ erg s^{-1} cm^{-2}).

We found that (not shown here) these hybrid simulations do not reproduce redshifted TR emission and the typical ribbon front profiles simultaneously.

5. Conclusions

In this work we have analyzed the spectral characteristics of the IRIS Mg II k, Mg II triplet, Fe XXI, and O IV lines in flare ribbons for four different flares, particularly focusing on the

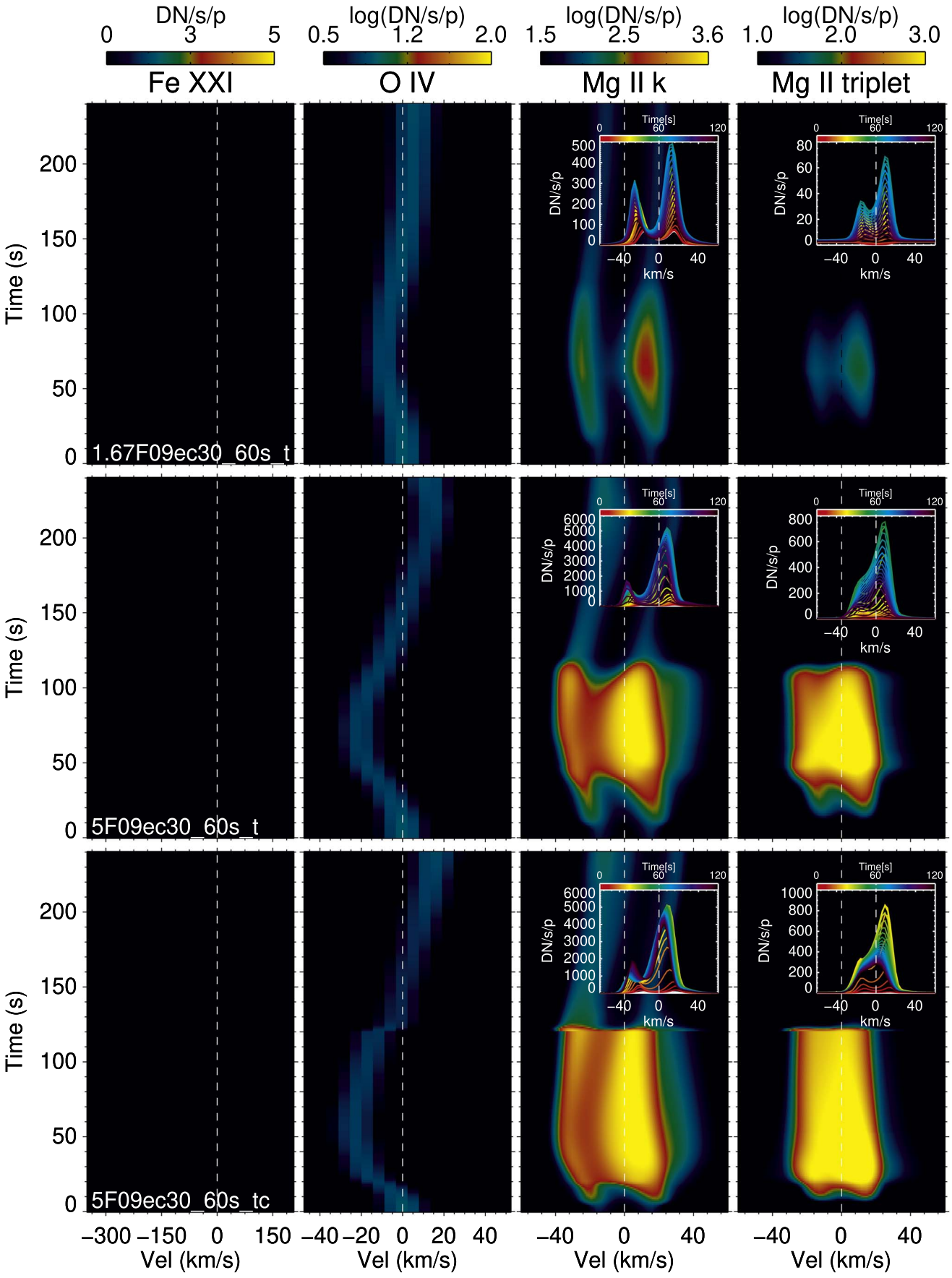

Figure 15. Long-duration simulations.

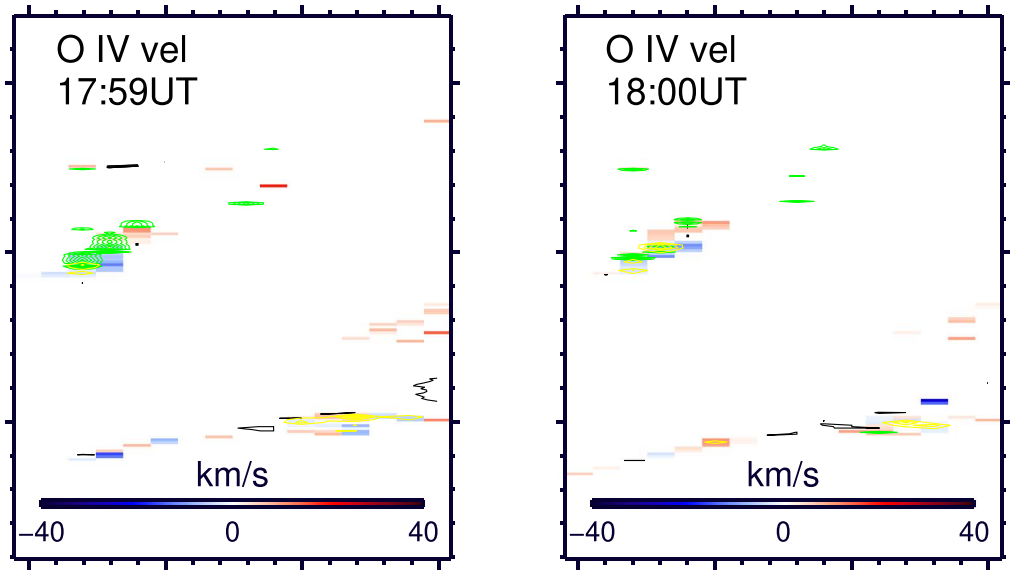

Figure 16. Example of O IV Doppler shift maps for two rasters during the 2015 June 22 flare (FL2). The green, yellow, and black contours show the location of the ribbon leading edge pixels, the maximum O IV intensity, and the maximum Fe XXI evaporation, respectively. See text for more details. A movie associated with this figure is also available. The movie has a duration of 7 s and consists of a sequence of individual figures identical to each of the panels in the figure above, showing the evolution of the Doppler shift maps from 17:51 UT to 18:10 UT.

(An animation of this figure is available.)

regional differences between the so-called leading edge and the main bright ribbon locations (Xu et al. 2016; Panos et al. 2018, 2021; Panos & Kleint 2021). We have quantified the spectral characteristics of the typical Mg II *k* profiles to allow a detailed comparison with radiative hydrodynamic simulations using the RADYN+FP and RH15D codes. We have also studied the correlation between the location of Mg II ribbon leading edge profiles and the intensity and flows observed in the Fe XXI line (the latter being a signature of chromospheric evaporation) and O IV TR line. The key results from our observational and modeling analysis can be summarized as follows:

1. The location of the ribbon front profiles in the IRIS Mg II chromospheric lines does not coincide most often with the location of strongest chromospheric evaporation and TR emission. In the flare with the highest cadence (FL3), we also note a small shift between the location of maximum evaporation and TR intensity.
2. Our RADYN+FP simulations suggest that heating models where the electrons have a more modest and gradual energy flux and higher E_C can qualitatively reproduce the observed enhanced Mg II central reversals and Mg II triplet emission but do not deposit enough energy to drive explosive chromospheric evaporation.
3. Models with larger flux and smaller E_C, which are better at driving explosive evaporation and heating of the TR, cannot explain the ribbon front profiles.
4. The optically thin O IV λ1401 line *can* be blueshifted in the ribbon front profiles, in agreement with our RADYN +FP models shown here. However, a more extensive analysis of optically thin O IV spectra for a larger sample of flares, possibly including ML analysis similar to that in the Panos et al. papers, would be needed to confirm our preliminary results.

One thing our models still cannot fully explain is the long duration (up to a few minutes) of the Mg II ribbon front profiles (e.g., Panos et al. 2018) and enhanced He I line absorption (Xu et al. 2016; Kerr et al. 2021). We are currently focused on addressing this issue as part of a follow-up paper (Kerr et al. 2023, in preparation).

Based on the results above, we propose that different heating processes might be at play in different regions of the ribbons at a certain time:

1. harder electron spectra but with a more gentle flux might be responsible for the enhanced reversal of the Mg II lines (in agreement with Kerr et al. 2021 for He I); and
2. different populations of accelerated electrons with higher fluxes and lower E_C drive chromospheric evaporation and the heating of the upper atmosphere.

It is not clear whether an evolution of the electron beam heating parameters over time might be able to explain both behaviors in a consistent way. We are aiming to address this question in Paper II (G. S. Kerr et al. 2023, in preparation). To summarize our results, in Figure 10 we suggest an updated version of the ribbon cartoon shown in Figure 1.

Finally, our work shows that by combining high-resolution observations by the IRIS spectrograph with advanced hydrodynamic simulations, we can obtain crucial constraints on the flare heating models. Future IRIS observations including recent very high (subsecond) cadence data sets[9] might soon reveal even more interesting and puzzling features in the evolution and characteristics of the ribbon front profiles.

V.P. acknowledges financial support from the NASA ROSES Heliophysics Guest Investigator program (grant No. NASA 80NSSC20K0716). G.S.K. acknowledges financial support from NASA's Early Career Investigator Program (grant No. NASA 80NSSC21K0460). V.P., G.S.K., and Y.X. acknowledge financial support from the NASA ROSES

[9] https://docs.google.com/document/d/1iPQPTYPULzrnjbnN38j6j0p2AccPTJc1xbqEXZmr0mU/edit

Heliophysics Supporting Research program (grant No. NASA 80NSSC19K0859). V.P. and J.L. acknowledge support from NASA under contract NNG09FA40C (IRIS). V.M.S. acknowledges the NSF FDSS grant 1936361. Y.X. acknowledges financial support from the SHINE grant (NSF-AGS-2228996). This manuscript benefited from discussions held at meetings of the International Space Science Institute team: "Interrogating Field-Aligned Solar Flare Models: Comparing, Contrasting and Improving," led by Dr. G. S. Kerr and Dr. V. Polito. IRIS is a NASA small explorer mission developed and operated by LMSAL with mission operations executed at NASA Ames Research Center and major contributions to downlink communications funded by the Norwegian Space Center (NSC, Norway) through an ESA PRODEX contract. CHIANTI is a collaborative project involving George Mason University (USA), the University of Michigan (USA), University of Cambridge (UK), and NASA Goddard Space Flight Center (USA). Resources supporting this work were provided by the NASA High-End Computing (HEC) Program through the NASA Advanced Supercomputing (NAS) Division at Ames Research Center.

Appendix
Additional Plots

In Figures 11–14 we show the synthetic spectra of Mg II *k* and Mg II triplet for all `RADYN+FP+RH15D` models. For the descriptions of the individual panels, see Figure 8 and text.

Figure 15 shows the synthetic spectra for the long-duration test simulations (see Section 4.2).

Finally, Figure 16 shows the O IV Doppler shift maps for two rasters during FL2 (see Section 4.3).

ORCID iDs

Vanessa Polito https://orcid.org/0000-0002-4980-7126
Graham S. Kerr https://orcid.org/0000-0001-5316-914X
Viacheslav M. Sadykov https://orcid.org/0000-0002-4001-1295

References

Allred, J. C., Alaoui, M., Kowalski, A. F., & Kerr, G. S. 2020, ApJ, 902, 16
Allred, J. C., Hawley, S. L., Abbett, W. P., & Carlsson, M. 2005, ApJ, 630, 573
Allred, J. C., Kowalski, A. F., & Carlsson, M. 2015, ApJ, 809, 104
Ashfield, W. H., & Longcope, D. W. 2021, ApJ, 912, 25
Asplund, M., Grevesse, N., Sauval, A. J., & Scott, P. 2009, ARA&A, 47, 481
Brosius, J. W. 2012, ApJ, 754, 54
Carlsson, M., Leenaarts, J., & Pontieu, B. D. 2015, ApJL, 809, L30
Carlsson, M., & Stein, R. F. 1995, ApJL, 440, L29
Cheung, M. C. M., Martínez-Sykora, J., Testa, P., et al. 2022, ApJ, 926, 53
De Pontieu, B., Polito, V., Hansteen, V., et al. 2021, SoPh, 296, 84
De Pontieu, B., Title, A. M., Lemen, J. R., et al. 2014, SoPh, 289, 2733
Del Zanna, G., Dere, K. P., Young, P. R., & Landi, E. 2021, ApJ, 909, 38
Dere, K. P., Landi, E., Mason, H. E., Monsignori Fossi, B. C., & Young, P. R. 1997, A&AS, 125, 149
Doschek, G. A., & Feldman, U. 1978, A&A, 69, 11
Dudík, J., Polito, V., Dzifčáková, E., Zanna, G. D., & Testa, P. 2017, ApJ, 842, 19
Emslie, A. G., Dennis, B. R., Shih, A. Y., et al. 2012, ApJ, 759, 71
Fisher, G. H., Canfield, R. C., & McClymont, A. N. 1985, ApJ, 289, 414
Fletcher, L., Dennis, B. R., Hudson, H. S., et al. 2011, SSRv, 159, 19
Fletcher, L., & Hudson, H. S. 2008, ApJ, 675, 1645
French, R. J., Matthews, S. A., Jonathan Rae, I., & Smith, A. W. 2021, ApJ, 922, 117
Goode, P. R., & Cao, W. 2012, in ASP Conf. Ser. 463, Second ATST-EAST Meeting: Magnetic Fields from the Photosphere to the Corona, ed. T. R. Rimmele et al. (San Francisco, CA: ASP), 357
Graham, D. R., & Cauzzi, G. 2015, ApJL, 807, L22
Graham, D. R., Cauzzi, G., Zangrilli, L., et al. 2020, ApJ, 895, 6
Holman, G. D., Aschwanden, M. J., Aurass, H., et al. 2011, SSRv, 159, 107
Huang, N., Sadykov, V. M., Xu, Y., Jing, J., & Wang, H. 2020, ApJL, 897, L6
Huang, N., Xu, Y., Sadykov, V. M., Jing, J., & Wang, H. 2019, ApJL, 878, L15
Janvier, M., Aulanier, G., Pariat, E., & Démoulin, P. 2013, A&A, 555, A77
Jeffrey, N. L. S., Fletcher, L., Labrosse, N., & Simões, P. J. A. 2018, SciA, 4, eaav2794
Kerr, G. S., Allred, J. C., & Carlsson, M. 2019a, ApJ, 883, 57
Kerr, G. S., Carlsson, M., & Allred, J. C. 2019b, ApJ, 885, 119
Kerr, G. S., Carlsson, M., Allred, J. C., Young, P. R., & Daw, A. N. 2019c, ApJ, 871, 23
Kerr, G. S., Fletcher, L., Russell, A. J. B., & Allred, J. C. 2016, ApJ, 827, 101
Kerr, G. S., Simões, P. J. A., Qiu, J., & Fletcher, L. 2015, A&A, 582, A50
Kerr, G. S., Xu, Y., Allred, J. C., et al. 2021, ApJ, 912, 153
Kobanov, N., Chelpanov, A., & Pulyaev, V. 2018, JASTP, 173, 50
Kontar, E. P., Brown, J. C., Emslie, A. G., et al. 2011, SSRv, 159, 301
Leenaarts, J., a, T. M. D., Carlsson, M., Uitenbroek, H., & De Pontieu, B. 2013a, ApJ, 772, 89
Leenaarts, J., Pereira, T., & Uitenbroek, H. 2012, A&A, 543, A109
Leenaarts, J., Pereira, T. M. D., Carlsson, M., Uitenbroek, H., & De Pontieu, B. 2013b, ApJ, 772, 90
Lin, R. P., Dennis, B. R., Hurford, G. J., et al. 2002, SoPh, 210, 3
Liu, C., Xu, Y., Deng, N., et al. 2013, ApJ, 774, 60
Liu, W., Heinzel, P., Kleint, L., & Kašparová, J. 2015, SoPh, 290, 3525
Lörinčík, J., Dudík, J., & Polito, V. 2022, ApJ, 934, 80
Naus, S. J., Qiu, J., DeVore, C. R., et al. 2022, ApJ, 926, 218
Panos, B., & Kleint, L. 2021, ApJ, 915, 77
Panos, B., Kleint, L., Huwyler, C., et al. 2018, ApJ, 861, 62
Panos, B., Kleint, L., & Voloshynovskiy, S. 2021, ApJ, 912, 121
Pereira, T. M. D., Carlsson, M., Pontieu, B. D., & Hansteen, V. 2015, ApJ, 806, 14
Pereira, T. M. D., Leenaarts, J., De Pontieu, B., Carlsson, M., & Uitenbroek, H. 2013, ApJ, 778, 143
Polito, V., Reep, J. W., Reeves, K. K., et al. 2016, ApJ, 816, 89
Polito, V., Testa, P., Allred, J., et al. 2018, ApJ, 856, 178
Polito, V., Testa, P., & De Pontieu, B. 2019, ApJL, 879, L17
Priest, E. R., & Forbes, T. G. 2002, A&ARv, 10, 313
Ramaty, R., & Mandzhavidze, N. 2000, in AIP Conf. Ser. 522, COSMIC EXPLOSIONS: Tenth Astrophysics Conference, ed. S. S. Holt & W. W. Zhang (Melville, NY: AIP), 401
Reep, J. W., Polito, V., Warren, H. P., & Crump, N. A. 2018a, ApJ, 856, 149
Reep, J. W., & Russell, A. J. B. 2016, ApJL, 818, L20
Reep, J. W., Russell, A. J. B., Tarr, L. A., & Leake, J. E. 2018b, ApJ, 853, 101
Rubio da Costa, F., & Kleint, L. 2017, ApJ, 842, 82
Sainz Dalda, A., de la Cruz Rodríguez, J., De Pontieu, B., & Gosic, M. 2019, ApJL, 875, L18
Sainz Dalda, A., & De Pontieu, B. 2022, arXiv:2211.05459
Tei, A., Sakaue, T., Okamoto, T. J., et al. 2018, PASJ, 70, 100
Testa, P., De Pontieu, B., Allred, J., et al. 2014, Sci, 346, 1255724
Tian, H., Young, P. R., Reeves, K. K., et al. 2015, ApJ, 811, 139
Uitenbroek, H. 2001, ApJ, 557, 389
Xu, Y., Cao, W., Ding, M., et al. 2016, ApJ, 819, 89
Xu, Y., Yang, X., Kerr, G. S., et al. 2022, ApJL, 924, L18
Young, P. R., Tian, H., & Jaeggli, S. 2015, ApJ, 799, 218
Zhu, Y., Kowalski, A. F., Tian, H., et al. 2019, ApJ, 879, 19
Zirin, H. 1980, ApJ, 235, 618